Optimization of painting efficiency applying unique techniques of high-voltage conductors and nitrotherm spray: Developing deep learning models using computational fluid dynamics dataset

Special Collection: Paint and Coating Physics

Mohammad-Reza Pendar ✉ ⓘ ; Sílvio Cândido ⓘ ; José Carlos Páscoa ⓘ

Check for updates

View Online   Export Citation   CrossMark

Articles You May Be Interested In

Evaluation of XHVRB for capturing transition to detonation as measured by embedded gauges

AIP Conference Proceedings (November 2020)

Gap test modeling to predict wedge tests initiation of PBXN-103

AIP Conference Proceedings (July 1998)

Sound rating of catalog air handlers

J Acoust Soc Am (March 2023)

Optimization of painting efficiency applying unique techniques of high-voltage conductors and nitrotherm spray: Developing deep learning models using computational fluid dynamics dataset

View Online   Export Citation   CrossMark

Mohammad-Reza Pendar,[a] (iD) Sílvio Cândido, (iD) and José Carlos Páscoa (iD)

AFFILIATIONS

University of Beira Interior, Department of Electromechanical Engineering, C-MAST (Center for Mechanical and Aerospace Sciences and Technologies) FCT (Portuguese Foundation for Science and Technology), Research Unit N° 151, Covilhã, Portugal

Note: This paper is part of the special topic, Paint and Coating Physics.
[a]Author to whom correspondence should be addressed: m.reza.pendar@ubi.pt. **Tel.:** +351925467631; **Fax:** +351275329972

ABSTRACT

The impetus of the current three-dimensional Eulerian–Lagrangian work is to analyze the impact of simultaneously using the inventive high-voltage conductors and Nitrotherm spraying technique for maximizing the industrial painting process efficiency. This investigation employs high-fidelity computational fluid dynamics (CFD) results in deep learning models as an input dataset. The novel conductors are called high-voltage retractable blades (HVRB) and high-voltage adjustable control-ring (HVACR) mounted on the head of the electrostatic rotating bell sprayer. The influence of dominant operational parameters, such as temperature and velocity of injected nitrogen or air, droplets' electric charge values, and their size ranges, and electric field density are examined in the considered database for the Nitrotherm spraying methodology. This broad range of parametric investigation illustrates that the inclusion of shaping nitrogen flow, manipulated electric field density, and droplet charging weights significantly affect the spraying deposition rate. The pressurized clean heated nitrogen flow, which is injected from the nozzles of the atomizers, positively redirects and harmonizes the charged droplets that construct an optimized spray plume pattern with a smaller diameter. Using innovative HVRB and HVACR conductors is manipulated the electric fields and leads to denser distribution, intensifying the acting electric force on the droplets, resulting in higher spraying transfer efficiency (TE) and thicker film formation. Based on the results, employing the introduced conductors in combination with the heated nitrogen instead of air leads to higher TE, rare overspray occurrence, formation of an esthetic paint film, lower paint consumption, and application time. Also, the collected complete database is employed for machine learning investigation to predict flow with high accuracy, aiming to reduce computational time/cost. A convolutional auto-encoder is used to reduce the computational cost with just 10% of the initial CFD computations, with a mean error of 1% on the prediction of the deposited droplet areas of the spray. The analysis revealed that by employing recurrent convolutional layers, superior capturing of the input pattern is obtained, which significantly aids the final prediction.

I. INTRODUCTION AND MOTIVATION

As the most remarkable energy consumer during industrial production, the paint shop plant needs specific attention to enhance energy efficiency while providing paint film with high physical qualities, such as corrosion resistance, surface durability, and mechanical protection (Akafuah *et al.*, 2016). Nitrotherm electrostatic spray-painting method with superior transfer efficiency (TE) up to 90% under an ideal condition is become a fundamental painting technology, particularly in the coating process of the automotive and aerospace industries (Pendar *et al.*, 2022). The primary objectives of this technology can be stated as shorter process times and the avoidance of undesirable phenomena, such as overspray, unsatisfactory film quality, excessive material usage, and significant pollution levels. Numerical modeling of the coating process using the electrostatic rotating bell sprayers (ERBSs) with optimization bases concepts need to be performed to meet the aforementioned requirements and expose a deep insight into turbulence airflow and

droplets traveling mechanisms. Nitrotherm electrostatic spraying also can be broadly employed in other significant applications of pharmaceutical industries (pill coverage), disinfection operations (microbial droplets removal from the polluted surface), agriculture pesticides, and crop dusting. This work aims to develop this approach by introducing two novel techniques, employing simultaneously the Nitrotherm spraying technique and high-voltage conductors mounted on the head of the ERBS to maximize the spraying process efficiency.

During the past two decades, some experimental and numerical research has considered the main spray coating characteristics, including the formation of film, ligament, and droplets inside the rotary bell cup, transportation of disintegrated droplets, and final film formation on the target. In numerical modeling, mainly Euler–Lagrange approach has been used compared to Euler–Euler method for spraying two-phase flow simulation.

Studies on electrostatic spraying are mainly focused on the areas of the electric field and charging process (I), employing high-voltage external conductor (II), droplets formation, disintegration, transportation, and deposition process (III), atomized droplets' breakup mechanism (IV) and evaporation procedures (V), spray droplet size distribution analyzing (VI), novel Nithrotherm spraying technique employing in electrostatic spraying (VII), which are extensively reviewed in the following paragraphs. Also, related published literature about employing the deep learning strategy in computational fluid dynamics (CFD) (VIII) has been addressed.

(I) Electric Field and Droplets Charging Process During Spraying: The effective implementation of the droplet charging process and electric field production is significant challenges in using the electrostatic sprayer. The droplet charging procedures as a critical determinant in the ERBSs' spray shape controlling are provided in Ellwood and Braslaw (1998). Im *et al.* (2001) assert that an effective application of an electric field enhances coating effectiveness. Ye *et al.* (2002) implemented a corona charge mechanism during the spraying procedure. Their evidence found that the particle size significantly depends on the space charge. Im *et al.* (2004) discovered that the shape of the spray plume is highly influenced by both the charge-to-mass ratio and the electric force. According to their findings, the total TE of the ERBS is around 44%, 90%, and 94% under zero voltage, −80, and −90 kV, respectively. Toljic *et al.* (2011) investigated various charge-to-mass ratios of droplets of varying sizes and realized that they had a significant effect on the resulted film by enhancing the TE. The OpenFOAM framework was used by Dastourani *et al.* (2018) to propose a numerical solution for modeling the electro-spraying process in the cone jet. The results showed good agreement with the experimental data, which supports the viability of the simulation methods for the electrospray phenomena. They revealed that the correlations of the liquid flow rate and electric potential could appropriately predict the establishment of the flow modes and vortices characteristics. Pendar and Páscoa (2019; 2020) evaluated the fundamental flow characteristics of the spraying in the ERBS, focusing on droplet charge, electric field, and ambient conditions. Their numerical analysis showed that the inclusion of droplet charging and electric field coupling, in different parametric values, significantly impacts the atomized droplet distribution over the spray plume and the deposition rate. They found a balance between the bell cup surface voltage and the droplet's charged values, revealing improvements in the TE and performance of the ERBS.

(II) High-voltage External Conductor and Related Patent: During the electrostatic spraying process, droplets can be electrically charged using either an external or internal methodology. In the internal/direct method, the supplied high-voltage DC to the applicator charges the liquid before injecting and atomizing. In the external/indirect approach, the high voltage is applied to a forward-facing electrode series (Domnick *et al.*, 2006). The external and internal charging techniques are appropriate for water-based and solvent-based paints because of the low and high solvent conductivities, respectively (Pendar *et al.*, 2022). Wang *et al.* (2006) presented an electrostatic spray gun that is combined with circular pattern electrodes, such as the sprayer's cup design to shape a circular cone spray plum or two linear electrodes to support the majority of the liquid particles in an aspect of electrical charging. Domnick and Thieme (2006) modified the electric field distribution by adding external symmetric corona needles to the electrostatic sprayer and discovered a positive effect on deposited film thickness and TE. Nolte *et al.* (2019) disclose electrode arrangement in support of an electrostatic atomizer, which is generated an electric field that assists in providing discharge currents flowing across a housing surface. An electrostatic atomizer with an electrode attached to the sprayer's head spot was proposed by Terebessy (2019). These electrodes were setup so that a counterbalanced quantity of the opposing electrical charge be produced to deal with the electrical charge of the sprayed liquid and appropriately direct them. Cooper (2021) introduces a spray dispersal feature that shortens the time needed for the paint cloud to hang after spraying. Their system includes a related sprayer cup with a nozzle to charge, atomize, and spray the injected liquid. Pendar and Páscoa (2021) proved the substantial influence of the voltage and appropriate external electric charging by employing a high-voltage ring shape conductor in the spray deposition rate. Mounting this conductor on the ERBS increased the TE value by around 10%. According to their findings, the moderate charge-to-mass ratio ($\rho_m^q \approx -1$ mC/kg) produced the highest TE.

(III) Droplets Formation, Transportation, and Deposition: The injected liquid disintegration, ionization, and electrical charging happen inside and close to the sprayer's head. Inside the rotary cup surface, the generated sheets disintegrate into fragments because of aerodynamic waves and then transform into ligaments due to surface tension. Then, elongated ligaments disintegrated into the distribution of the non-uniform droplets farther from the cup's rim. According to Domnick and Thieme (2006), the fragment pattern evolved less consistently as the bell cup's rotational speed boosted. Liu *et al.* (2012) correlated the equation for droplet size after examination of ligament and droplet generation mechanisms over a wide range of operational settings. Soma *et al.* (2015) assessed the liquid film behavior on a rotating bell surface and reported the thickness of the film near the bell edge. Moore (2017) assessed the disintegration process between ligaments and droplets during employing serrated and non-serrated rotary cups at different paint flow rates. Also, Shen *et al.* (2019) experimentally evaluated the liquid film formation inside the rotary cup with obtained a series of snapshots.

(IV) Droplets Breakup During Electrostatic Spraying: The breakup process, subjecting injected paint liquid to the robust centrifugal force due to the bell cup rotation in an electrostatic sprayer, is a critical phenomenon that needs consideration. This process is divided into two main modes, primary and secondary. In the primary mode, the diameter and angle of the droplets inside the rotary bell cup are

determined, and rim deformation and expansion of droplets occur (Jackiw and Ashgriz, 2021). The secondary breakup procedure is a prominent phenomenon when the droplets travel from the bell cup to the workpiece (Im *et al.*, 2001). Recently, Rosin–Rammler and Chi-squared models have been broadly employed to predict the initial distribution of droplets during electrostatic spraying. The first one is more accurate compared to the experimental distribution (Pendar and Páscoa, 2020). The strength of different efficient secondary breakup models, including the Reitz-Diwakar, Reitz-KHRT Hybrid, Pilch-Erdman, Taylor analogy breakup (TAB), and modified TAB, are explained and examined in electrostatic spraying in the study by Pendar and Páscoa (2020). Using a rotary bell sprayer, Shen *et al.* (2017) encountered difficulties with the droplets' primary breakup, film generation, and propagation inside the rotary bell.

(V) Evaporation Process in Spraying: The evaporation of droplets and their heat transfer during electrostatic spraying is precisely modeled in references of Arumugham-Achari *et al.* (2015) and Shrimpton and Laoonual (2006). The application of the electric charge and its impact on the droplet's evaporation process were addressed by Brentjes *et al.* (2020). Pendar and Páscoa (2021) evaluated the droplets' energy balance during evaporation in electrostatic spraying using Ranz and Marshall approach. Also, the droplets' temperature is described in detail by Dbouk and Drikakis (2020) via computing complete solving energy and enthalpy equations.

(VI) Spray Size Distribution Analyzing in Spraying: The produced droplet size distribution by the considered types of the sprayer in the current work, the ERBSs, significantly affects the TE and finish quality. Better quality was produced with smaller droplet sizes and lower TE, whereas the opposite was true with larger size dispersion (Pendar *et al.*, 2022). The dominant parameters influencing the distribution of droplet size in electrostatic sprayer operation are injected cup's rotational speed, liquid paint flow rate, inlet air flow rate, and rotary cup design (Ray *et al.*, 2019). Some basic works, such as Ellwood and Braslaw (1998), confirmed droplet size reduction by growing the rotational speed while increment by increasing the paint flow rate. Yasumura *et al.* (2011) revealed an impressive effect of electric voltage on medium-size of droplets diameter ($d_p \approx 10$–$40\,\mu m$). Ahmed and Youssef (2012) clarified the impact of the Reynolds number, Weber number, and flow coefficient on the Sauter mean diameter ($SMD = \sum N_i D_i^3 / \sum N_i D_i^2$) as a meaningful metric for defined droplet size distribution. N_i and D_i denote the droplet numbers in the ith size range and diameter. Ahmed and Youssef (2014) worked on the size of the droplets produced during the disintegration as well as describing the transition process among the film, ligament, and droplets. Wilson *et al.* (2018) visualized ligament and droplet formation and proved the SMD decrement, one quarter, at the maximized rotational speed. The phenomena of non-Newtonian droplets disintegration were studied by Shen *et al.* (2019). Oswald *et al.* (2019) illustrated the effect of the elongational resistance on the disintegration procedure inside the sprayer's rotary bell cup. Droplet size distribution prediction in electrostatic sprayer operation still is ambiguous and requires more attention.

(VII) Nithrotherm Spraying Technique: The technology of using heated nitrogen in an electrostatic spraying process is already experienced in rare high-tech companies, and very positive results have been observed. Spang (2014) briefly explained the spray coating using heated nitrogen and compared it with conventional spraying using air. They reported improvement in the transfer efficiency (TE) value and faster paint curing time. Bensalah *et al.* (2014) announced the higher transfer efficiency for the Nitrotherm coating method. This approach can develop the paint shop's energy and material consumption. Recognizing the mentioned technologies process is still ambiguous that described in the current study.

(VIII) Deep Learning: A powerful method for improving comprehension and fluid flow behavior prediction is using machine learning models in conjunction with computational fluid dynamics (CFD) simulations, especially in industrial applications like the present work. This helps in lowering the computational cost of running complete CFD simulations. Computational fluid dynamics has revolutionized thanks to recent advances in machine learning. One typical strategy is to utilize machine learning models to predict fluid flow behavior based on a small set of input variables, such as boundary conditions or beginning circumstances (Kochkov *et al.*, 2021). Convolutional neural networks (CNNs) and recurrent neural networks (RNNs), as two prominent machine learning models, have demonstrated promising results in CFD applications (Yang, 2008). For instance, CNNs have been used to predict turbulent flows accurately (Kim *et al.*, 2022), ANN to analyze the nanofluids jet impingement heat transfer and pressure drop in the microchannel heat sink (Naphon *et al.*, 2019), or even radial basis neural network (RBFNN) is developed and employed to model the pressure drop for cyclone separator (Elsayed and Lacor, 2011). These models can automatically extract spatial information from the input data and learn complex fluid dynamics patterns by utilizing the convolutional layers of CNNs. On the other hand, it has been demonstrated that RNNs are useful for modeling temporal relationships in data related to fluid flow (Brunton *et al.*, 2016). These models can record the fluid flow's temporal evolution using recurrent layers and generate predictions based on the flow's past behavior enhanced super-resolution generative adversarial network (GAN) is applied as a model to reconstruct the high-resolution velocity fields, which are constituted by CNN models (Yousif *et al.*, 2022), to map spatially limited turbulence to high-fidelity data (Yousif *et al.*, 2021). Convolutional architecture remains dominant in most computer vision tasks, such as objection, image classification, and video prediction. Thanks to their efficiency and desired inductive biases, e.g., locality and translation equivariance, convolution neural nets have been widely applied to emulate and predict complex spatio-temporal physical dynamics. Here, we propose a deep learning method for forecasting fluid flow behavior using a constrained set of input variables. The spatial and temporal properties in the fluid flow data are specifically captured using convolutional models. To increase the effectiveness and accuracy of the models, cutting-edge techniques are applied, such as transfer learning with recurrent learning cells. The performance of the applied method to other cutting-edge techniques is compared while evaluating it on a real-world CFD dataset.

This paper's structure is as follows: Sec. II explains the mathematical model and the numerical implementation used for simulations. Also, this section provides information on different considered electrostatic sprayers' design configurations and describes the simulation settings. Section III concentrates on analyzing the results obtained by CFD simulating and deep learning modeling, and finally, Sec. IV presents concluding remarks.

II. SIMULATION METHODOLOGY

A. Governing equations

Here a three-dimensional (3D) comprehensive Eulerian–Lagrangian algorithm is extended under the framework of the OpenFOAM package to provide an in-depth analysis of the fully turbulent airflow field with the presence of heated nitrogen-enriched distribution (I), electric field generation and droplets charging process (II), dynamics and trajectory tracking of manipulated droplets (III), primary and secondary breakup processes (IV), atomized liquid evaporation (V), and deposited film structure and thickness (VI). An unsteady compressible Navier–Stokes solver is combined with a Large Eddy Simulation (LES) model to precisely simulate the turbulence effects of the air or nitrogen flow field on the droplets.

(I) Continuous Phase: The Favre average compressible equations of Navier–Stokes (NS) by applying the LES filtering method are used in this work to model the airflow. We assume a compressible flow due to the existence of supersonic flow regimes near the rotary bell cup surface. The LES turbulence approach is designed to calculate the larger and energy-rich eddies while modeling the smaller sub-grid all over the computational domain. This model can handle the stress rate and high strain of complex flows inside and around the sprayer's head. When using LES, all variables are separated into grid scale (GS) ($\bar{f}$) and sub-grid scale (SGS) (f') components, which express as $f = f' + \bar{f}$. The grid-scale component is defined as $\bar{f} = G * f$, where $G = G(X, \Delta)$ and $\Delta = \Delta(X)$ are denoted by the filter function and filter width (Ghosal, 1996). The top-hat filter (De Villiers, 2006), an implicit filter affiliated with the grid spacing that control whether the minor scales are contained, has been used here under the framework of the OpenFOAM source code:

$$G(x, \Delta) = \begin{cases} 1/\Delta : & \text{if } (x \le \Delta/2) \\ 0 : & \text{otherwise.} \end{cases} \quad (1)$$

The grid spacing is employed to set the filter width Δ (De Villiers, 2006). Here, the scales below the length of the filter width Δ are modeled and a "smooth" delta is used, which is explained in detail in Roohi et al. (2016). The smoothed distribution gradient is fixed by interfering with the adjustable coefficient ($C_{\Delta S}$) to the filter width $\Delta = \max(\Delta_P, \Delta_N/C_{\Delta S})$. N and P are the definition of neighbor cell and present cell, respectively. The function of G convolved the NS equations and the following filtered continuity and momentum equations are used in the LES model:

$$\frac{\partial \bar{\rho}}{\partial t} + \frac{\partial (\bar{\rho}\, \bar{u}_j)}{\partial x_j} = 0, \quad (2)$$

$$\frac{\partial (\bar{\rho}\bar{u}_j)}{\partial t} + \frac{\partial (\bar{\rho}\bar{u}_i\bar{u}_j)}{\partial x_j} = -\frac{\partial \bar{p}}{\partial x_i} + \frac{\partial \bar{\sigma}_{ij}}{\partial x_j} - \frac{\partial \tau_{ij}}{\partial x_j} + f_{st} + f_{es} + S. \quad (3)$$

p is pressure and $\tilde{\sigma}_{ij}$ is the viscous stress tensor, which is defined as

$$\tilde{\sigma}_{ij} = \bar{\mu} \left(\frac{\partial \tilde{u}_i}{\partial x_j} + \frac{\partial \tilde{u}_j}{\partial x_i} - \frac{2}{3} \delta_{ij} \frac{\partial \tilde{u}_k}{\partial x_k} \right), \quad (4)$$

δ_{ij} and $\bar{\mu}$ denote the Kronecker delta function and kinematic viscosity, respectively. The body forces of surface tension (f_{st}), electric stress (f_{es}) and other operating forces like gravity (S) are added to the above formula. The unresolved transport element, τ_{ij} as a SGS is defined as

$$\tau_{ij} \approx \bar{\rho} \left(\overline{u_i u_j} - \overline{u_i}\,\overline{u_j} \right). \quad (5)$$

The above formula is modeled using an eddy-viscosity sub-grid approach as follows:

$$\tau_{ij} = \frac{2}{3} \bar{\rho} k I - 2\mu_k \overline{S_{ij}}, \quad (6)$$

$$\overline{S_{ij}} = \frac{1}{2} \left(\frac{\partial \overline{u_i}}{\partial x_j} + \frac{\partial \overline{u_j}}{\partial x_i} \right). \quad (7)$$

$\overline{S_{ij}}$ is the rate-of-strain tensor of resolved scale and μ_k is sub-grid scale turbulence viscosity obtained by the "Local Eddy-Viscosity" approach. Here, the "One Equation Eddy Viscosity (OEEV)" SGS model is used as follows:

$$\partial(\bar{\rho}k) + \nabla \cdot (\bar{\rho}k\tilde{u}) = -\tau_{ij} \cdot \overline{S_{ij}} + \nabla \cdot (\mu_k \nabla k) + \bar{\rho}\varepsilon, \quad (8)$$

$$\mu_k = c_k \bar{\rho} \Delta \sqrt{k}, \quad \varepsilon = c_\varepsilon k^{3/2}/\Delta, \quad (9)$$

where c_k and c_ε as two constants are set as 0.094 and 1.048 in the current code. Detailed analysis of various SGS models can be found in the study by Zahiri and Roohi (2019) and LarKermani et al. (2018).

(II) Electric Field Generation: The electric field is produced by the potential difference between high-voltage surfaces, highly negatively charged, near the liquid injection nozzle, and positively charged workpiece. The relation among the potential (φ) and space charge density (ρ^q) is modeled by using the Poisson equation:

$$\nabla^2 \varphi = -\frac{\rho^q}{\varepsilon'}. \quad (10)$$

The electric field intensity ($\vec{E}$) and charge of each particle (Q_i) are computed as follows:

$$\vec{E} = -\nabla\varphi, \quad \varepsilon' \nabla \cdot E = \rho^q, \quad (11)$$

$$Q_i = m_{P_i} \rho^q_{m_i} = (\rho_P V_{P_i})\rho^q_{m_i}, \quad (12)$$

ε', ρ_P, $\rho^q_{m_i}$, and V_{P_i} are air electrical permittivity, and density, charge to mass ratio and volume of each individual droplet. It needs to be noted that Q_i and ρ^q have different unit of charge and charge per unit volume. Finally, the electric force per unit mass (F_E), which defines ion wind airflow (electric field) effects on moving droplets:

$$F_E = q_{P_i} E = m_{P_i} \rho^q_{m_i} E, \quad E \cdot \nabla \rho^q = -\frac{\rho^{q2}}{\varepsilon'}. \quad (13)$$

m_{P_i} and q_{P_i} are individual droplet mass and charge, respectively.

(III) Discrete Phase of Droplets (Two-way Coupling with Continuous Phase): The discrete phase of the charged droplets' motion in the air/nitrogen flow is solved in the Lagrangian frame using differential equations and force balance integration based on Newton's law. The influential forces on droplets' trajectory that include Stokes drag (f_D), gravity (f_G), electric (f_E), and added-mass (f_M) forces express as follows:

$$\vec{F}_P = m_p \frac{\partial \vec{u}_p}{\partial t} = \frac{3}{4} C_d \frac{\rho_f}{\rho_P} \frac{m_P}{2R_P} |(\vec{u}_f - \vec{u}_P)|(\vec{u}_f - \vec{u}_P)$$
$$+ (\rho_P - \rho_f)V_P\vec{g} + \vec{E}q_P + \frac{\rho_f V_P}{2} \frac{\partial (\vec{u}_f - \vec{u}_p)}{\partial t}, \quad (14)$$

$\vec{u}_P$, $\vec{u}_f$, ρ_P, and ρ_f are the particle and fluid velocity vector and density, respectively. Also, V_P, R_P, m_P, and q_P are the volume, radius, mass

and the charge of the droplets, respectively. The drag coefficient (C_D) that depends on Reynolds number of droplets ($Re_p = 2R_P|\vec{u}_f - \vec{u}_p|\rho_f/\mu_f$) define as follows:

$$C_D = \begin{cases} 24/Re_P, & if \ \ Re_P < 1 \\ (24/Re_P)(1+0.5Re_P^{0.687}), & if \ \ 1 \leq Re_P \leq 1000 \\ 0.44, & if \ \ Re_P > 1000, \end{cases} \quad (15)$$

$\vec{\mu}_f$ is the fluid (air) dynamic viscosity.

(IV) Breakup Models: Breakup modeling, as the most critical phenomenon during the spraying procedures, is divided into two sets, primary and secondary. Here, the Rosin–Rammler distribution ($Y_d = \exp\left(-d/\bar{d}\right)^n$) is employed for the primary breakup modeling to determine the droplet's diameter and angle inside the rotary bell cup. The modified table breakup method is applied for the secondary breakup procedure modeling. This approach characterized based on the Weber number ($We = \rho u_{rel}^2 D_P/\sigma$). In this model, the parent droplets depend on product generation rate ($dn(t)/dt$) and proportional constant (k_{br}) breaks into product droplets, as follows:

$$dn(t)/dt = -3K_{br}n(t), K_{br} \begin{cases} k_1\omega & if \ We \leq We_t \\ k_2\omega\sqrt{We} & if \ We > We_t. \end{cases} \quad (16)$$

The k_{br} value is dependent on the breakup regime and parent properties, and transient Weber number (We_t) is set as 100 for the present computation. Also, k_1 and k_2 are perfectly adapted to the droplet velocity and size based on the experiment ($k_1 \approx k_2 = 0.2$) (Pendar and Páscoa, 2020). The product droplet distribution has been assumed as

$$\frac{r_{product}}{r_{parent}} = e^{-K_{br}t}, \quad (17)$$

r_{parent} and $r_{product}$ are the parent and product droplets radius. More details about this model are provided in our previous work, Ref Pendar and Páscoa (2020).

(V) Energy Evolution and Evaporation Process of Droplets: The temperature evolution of droplets is calculated by the following energy equation:

$$m_p c_p \frac{dT_p}{dt} = A_p(h(T_f - T_p) + \dot{q}_{abs} - \sigma \varepsilon T_p^4), \quad (18)$$

c_p, A_p, σ, h, and ε are the specific heat capacity and surface of droplets, Boltzmann constant, heat transfer coefficient, and radiation emissivity, respectively. Ranz–Marshall heat transfer method (Ranz and Marshall, 1952) is used to evaluate a paint droplet's mass due to the evaporation procedure. The Nusselt number and droplet diameter are used to calculate the heat transfer coefficient ($h = Nu_k/d_p = (2 + 0.6\sqrt{Re}Pr^{1/3})\kappa/d_p$).

(VI) Deposited Film Formulations: The mass conservation, momentum, energy, and thickness formulations of constructed film during the spray droplet deposition on the target are described in detail in the study by Pendar and Páscoa (2021).

B. Problem description

(I) Conceptual Explanation of Approach: Fig. 1 shows a schematic of the Nitrotherm electrostatic spray-painting procedure by
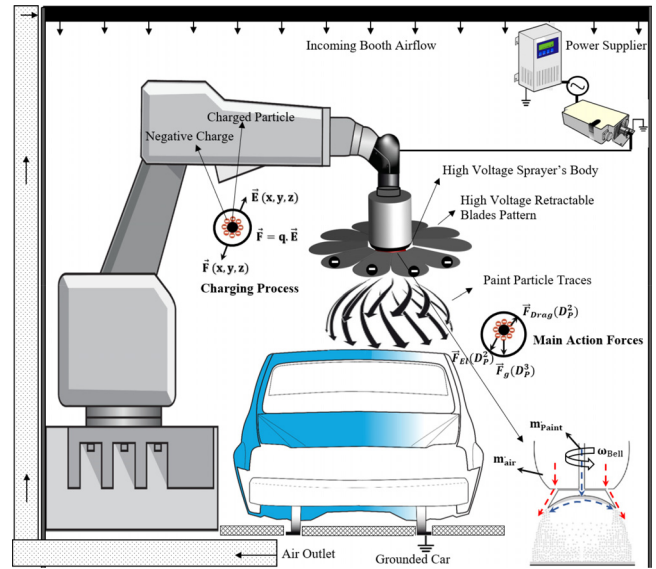

FIG. 1. Schematic description of the introduced forces during the general Nitrotherm electrostatic spray-painting mechanism.

means of the ERBS. The main forces which interact on the charged paint droplets during the traveling from the sprayer to the target are described in this figure. These dominant forces are (a) the electric force resulting from the electric field inclusion on the charged droplets in between the sprayer to target distance, (b) the centrifugal force produced by the rotation of the sprayer's bell cup, (c) the shaping airflow force produced by ninety nitrogen/air nozzles around the bell cup, deflects spray to ensure an axial flow toward the target, (d) drag, and (e) gravity forces. The obtained fine and consistent disintegrated droplets achieve a high-quality finished target surface by balancing these factors.

(II) Sprayers Characteristic and Boundary Conditions: Fig. 2 describes the dimensions and applied boundary conditions over the whole computational domain [Fig. 2(a)]. The structure of the conventional electrostatic sprayer [Fig. 2(b)] with the novel design supplements of high-voltage retractable blades (HVRB) [Fig. 2(c)] and high-voltage adjustable control-ring (HVACR) [Fig. 2(d)] conductors are also demonstrated. The HVRB conductor based on innovative design can be easily configured in semi-closed [Fig. 2(c_1)] and then fully closed [Fig. 2(c_2)] modes. Also, the diameter of the HVACR can be controlled by adjusting the designated pins level based on the required operating phase of spraying [Fig. 2(d)]. An ERBS, which was designed and commercialized by SAMES (SAMES Technology, 2019), is employed as a base sprayer for development purposes. The diameter of the sprayer's rotary bell cup, D = 65 mm, is used as the reference for non-dimensionalizing all reported dimensions in Fig. 2. The computational domain size is set as a cylinder with a diameter and height of 40 and 12D to ensure the flow is fully developed. The introduced atomizing system in Fig. 3 is employed to examine the effect of using heated nitrogen instead of air in a method called Nitrotherm electrostatic spray is considered. This simplified designed geometry and setup reduces the computational costs while still overall meeting the flow physics similar to what is considered in Fig. 2.

08 September 2023 13:45:49
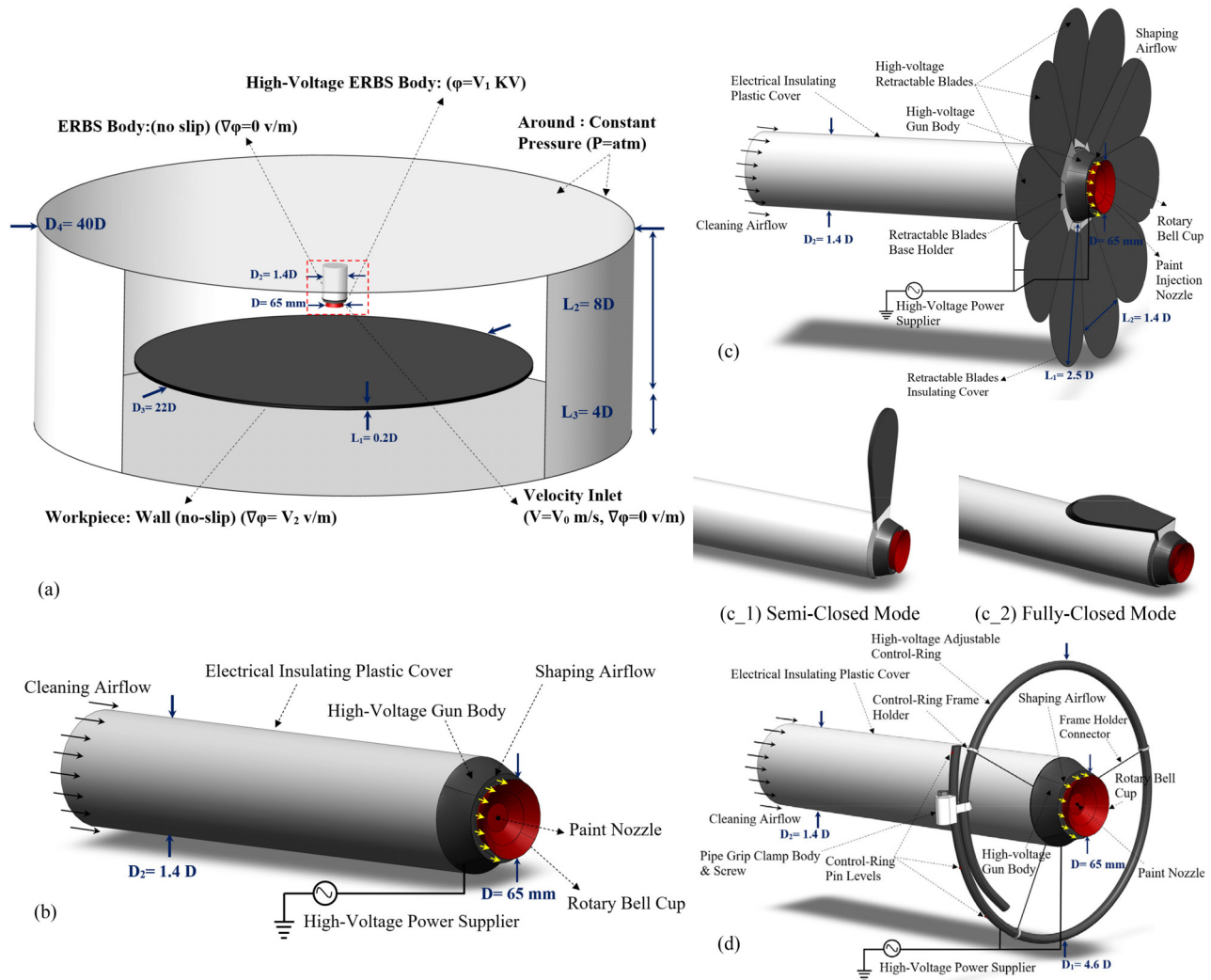
FIG. 2. Schematic drawing of the overall computational domain's dimensions and boundary conditions (a). Detailed description of ERBS's head design including: Conventional (b), with high-voltage retractable blades (HVRB) conductor (c) [Semi-closed mode (c_1), Fully closed mode (c_2)], and adjustable control-ring (HVACR) conductor (d).

The computational domain for the Nitrotherm electrostatic spray scenario (Fig. 3) is a cylinder with 540 and 70D of diameter and height, where D = 2.5 mm is the diameter of the liquid injection nozzle used for normalization. To provide an appropriate time step, ensure high precision results and faster convergence, the Courant number is kept below 0.45 to satisfy the time step around 1×10^{-7} s. The atmospheric boundary condition is set for defining the computing domains outside borders similar to real conditions. The surfaces of the sprayer's body, workpiece, HVRB, and HVACR conductors are applied as a condition of no-slip walls. A moving wall boundary is also considered for the rotary bell cup. A paint liquid jet with a diameter of D = 2.5 mm and a constant flow rate is supplied inside the bell cup center. The velocity inlet condition ($U_{Nozzles}$) is used for the nitrogen/air nozzle injector surfaces. A specific potential value ($\Phi = V_1$) is defined for the HVRB/HVACR conductors, inside the bell cup surface and stainless steel retaining collar surfaces for electric field boundary conditions. The

potential values in all other boundaries are set as zero value $\Phi = 0$. The specific charge-to-mass ratio (ρ_m^q) values are also applied to the surface of the disintegrated droplets. The boundary condition for the Nitrotherm electrostatic spray case is also specified in Figs. 3(a) and 3(b). For simplicity, water ($\rho_P = 998 \, \text{kg/m}^3$) is used as the paint surrogate, an identical approach can be seen in different references like Darwish Ahmad *et al.* (2018) and Viti *et al.* (2010). Also, the atmospheric air with density (ρ_{air}) of 1.225 kg/m³ is considered.

(III) Map of Considered Cases: The optimization-based framework's progressive steps of the current study are illustrated in Fig. 4. This figure also introduced all cases that are evaluated (52 cases for first idea and 18 cases for second idea) and examined dominant parameters over a broad range. The collected database aids in reaching a better understanding of the process physics. In the formation of a database for Nitrotherm electrostatic spray analysis for employing in deep learning (DL) and CFD purposes, the parameters of nitrogen/air
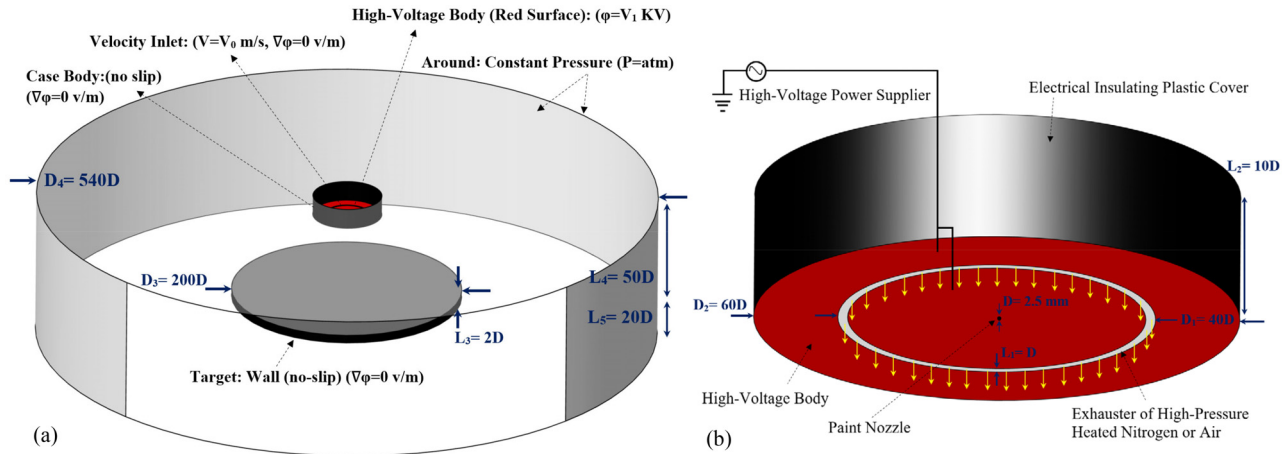
FIG. 3. The dimensions and boundary conditions of the configured designed geometry for the Nitrotherm spray technique analysis (a). Zoomed visualization of the geometry (b).

temperature (T), velocity (V), voltage of influential surface (φ_0), droplets charge-to-mass ratio (ρ_m^q), and size ranges (D_P) are considered. In the database for analysis of spraying using designated conductors, HVRB and HVACR, the parameters of the cup and conductor voltage (φ_{Cup}, $\varphi_{Conductor}$), droplets charge-to-mass ratio (ρ_m^q), rotational speed (ω_{bell}), airflow rate (m_{air}), and size ranges (D_P) are explored in a wide range.

We used the heated nitrogen electrostatic spray computations (a total of 26 cases) to integrate the CFD database and the machine learning models. For these cases, we extracted the number N of time steps, each containing information on the droplet's size, velocity, temperature, and spatial position, as well as a 2D cross section of the continuous phase velocity. The database passes through a preprocessing step,
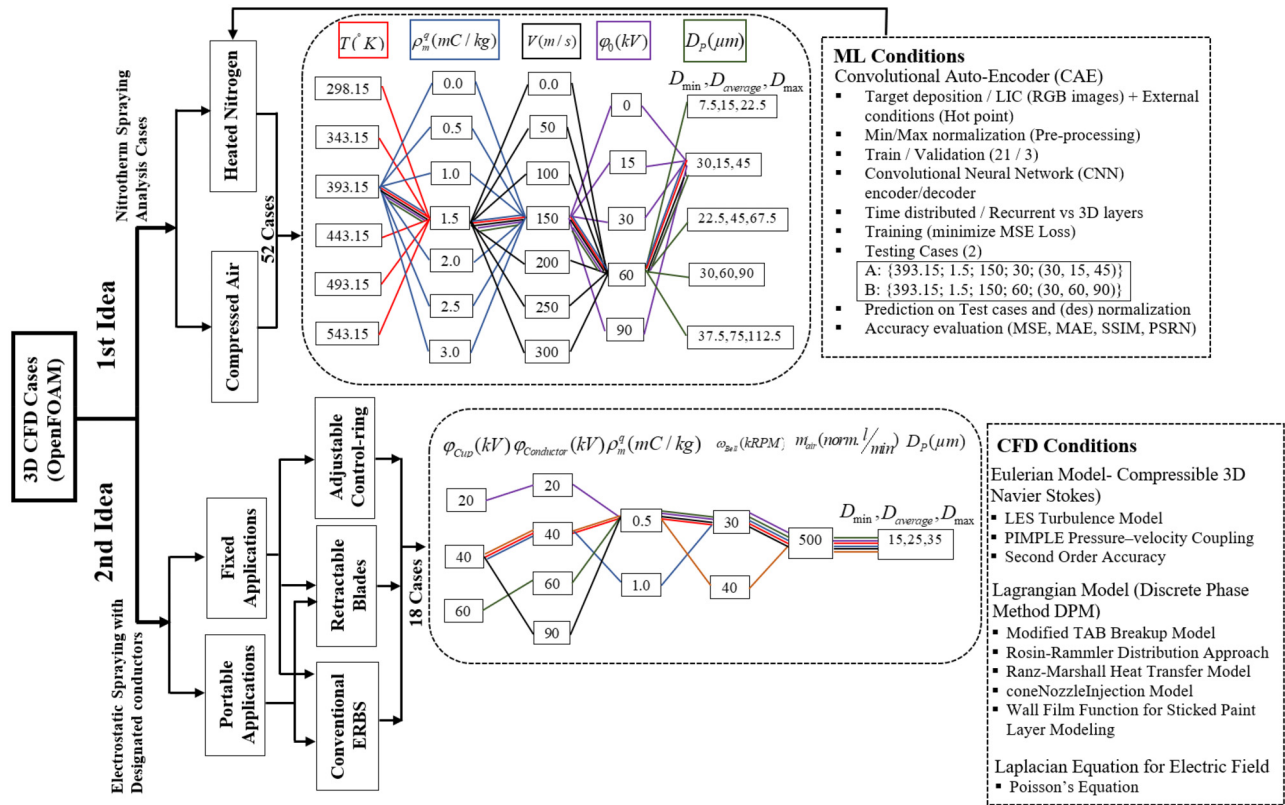

FIG. 4. Progressive steps and solutions for the electrostatic and Nitrotherm spraying analysis that are considered in this current study.

which consists of normalizing the flow variables by their maximum/minimum values. This ensures that the magnitudes of the values are comparable and promotes better learning for the machine learning model.

Figure 5 shows the manipulated practical electric field areas generated using the revolutionary HVRB or HVACR conductor systems in addition to the conventional ERBS. An appropriate balance must be maintained between the droplets' charge values and the strength and distance of the produced electric field equipotential lines distribution. The contours demonstrate larger covered areas with more robust potential distribution in the proposed cases with the HVRB and HVACR [Figs. 5(b) and 5(c)]. The dense electric fields, especially in the case of HVRB, are extended enough to fully cover the regions between the sprayer and workpiece at a scope of 0.25 m distance and accelerate the droplet transfer process. Features of the HVRB and HVACR adjustability and determination capability of negative voltage absolute value ranges significantly help to control spray plume, broader or narrower formation of the coverage regions. The tilting angle ($\Delta\alpha°$) in the ERBS with HVRB and the ring circumference difference (ΔL) in the ERBS with HVACR can be easily adjusted [see Figs. 5(b) and 5(c)]. These two supplements have no voids or gaps in the electric potential distribution. This improvement causes higher effective electric force values, as well as an increment in the TE, to be achieved, which will be discussed in Sec. III.

Figures 6(a) and 6(b) represent the produced Nitrotherm and electric fields between the liquid nozzle and target around the simplified designated geometry. The high-velocity nitrogen is injected through a circular layer with a diameter and thickness of 0.1 and 2.5 mm. These fields' strength and coverage region are manipulated due to varied operational conditions described in the diagram of Fig. 4.

(IV) Model Setup and Discretization Methods: Details of the discretization schemes used to achieve the precise results of the current work are provided in Table I. For the discretization of all terms, second-order accuracy is taken into account and a convergence target of 1×10^{-6} is considered. In this simulation analysis, the PIMPLE algorithm—a hybrid of the PISO (Issa, 1986) and SIMPLE (Patankar and Spalding, 1983) algorithms—is used for the pressure–velocity coupling. This approach provides superior stability and a fast convergence rate for larger time step values and greater coupling applicability in this Eulerian–Lagrangian simulation, employing the SIMPLE and PISO for the outer and inner corrector loops (Pendar and Páscoa, 2019). Here, the wall treatment employed in the LES turbulence modeling under the OpenFOAM framework (see Table I) relies on the values of the y^+ near-wall cells. The definition of the dimensionless wall distance is $y^+ = (u_\tau \cdot \Delta y)/v$, where u_τ, Δy, and v are the friction velocity, nearest distance to the wall surface and kinematic viscosity, respectively. The used wall functions will be activated only in the $y^+ > 11$ (Liu, 2016). The residuals of pressure and velocity reach around 10^{-8} and 10^{-9}, respectively. By analyzing the turbulent kinetic energy power spectrum density (PSD) at a location near the ERBS's rim, the Kolmogorov power law-decay ($f^{-5/3}$) indicates the statistical scaling accuracy to evaluate the flow field inertial scales.

(V) Computational Grid Analysis: Fig. 7 presented a complete visualization of a 3D fully structured quadrilateral grid produced over the three various sprayers of the conventional ERBS (b) and (c), ERBS with HVRB conductor (d), and the ERBS with HVACR conductor (e). Based on the grid independency study in the previous studies of the authors for the conventional ERBS (Pendar and Páscoa, 2019; 2020), between three different generated grids within overall cells of 5.5, 8.5,
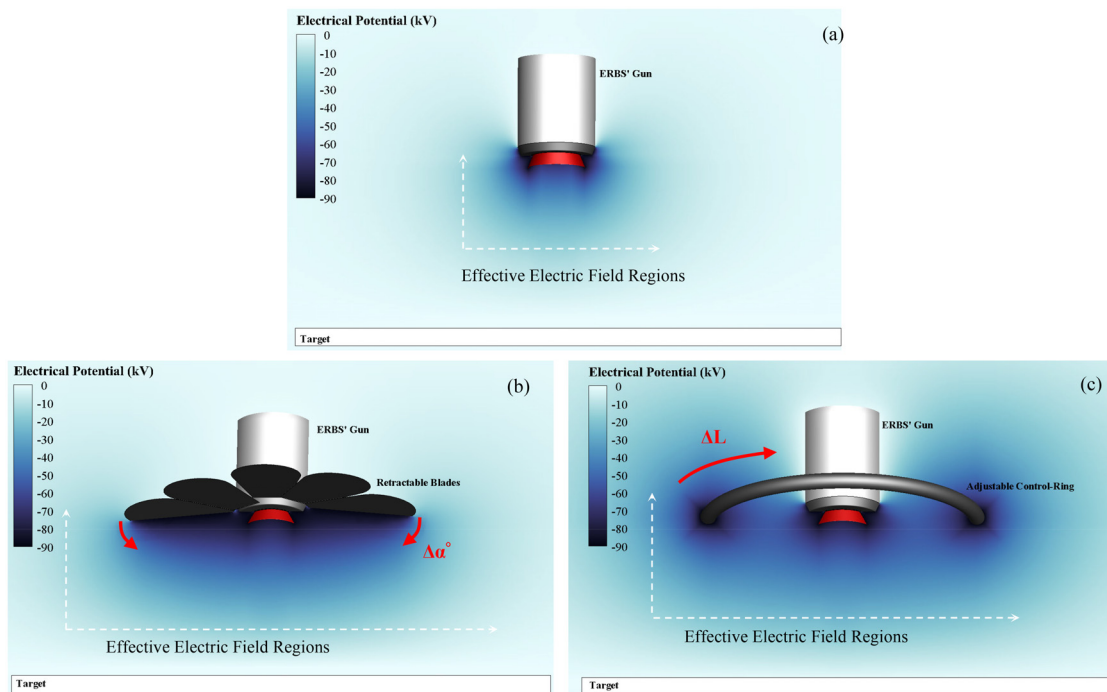

FIG. 5. Representation of generated electric field distribution around the conventional ERBS (a), with HVRB conductor (b) and HVACR conductor (c).
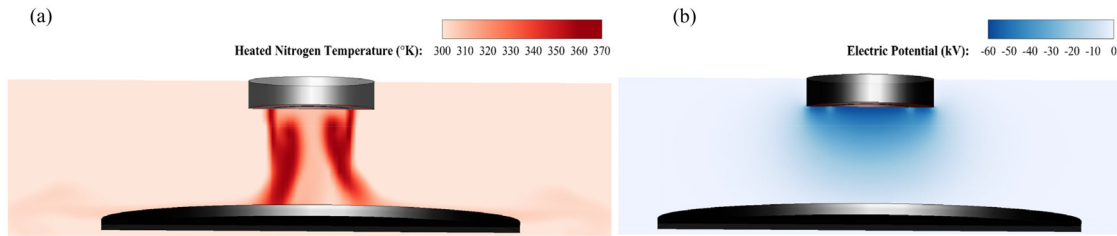
FIG. 6. Produced distribution of the heated nitrogen-enriched (a) and electric field (b) around the simplified designated geometry.

TABLE I. Summary for discretization schemes implemented in the current study.

| Discretization	Schemes	Description/comments
Time schemes	Backward difference	Second order, implicit
Pressure–velocity coupling	PIMPLE	Hybrid of SIMPLE- PISO algorithms
Spatial discretization	Gradient Gauss linear	Second order (Gaussian integration), Linear interpolation (central differencing)
	Divergence—Gauss upwind	Second order unbounded (Gaussian integration), Upwind differencing
	Laplacian surface normal gradient—Gauss linear corrected	Unbounded, second order, conservative
Wall functions	ν_t—nutkWallFunction	Serves as a condition with zero gradient for the modeled k
	K—kqRWallFunction	develops a ν_t near-wall profile using a modeled k
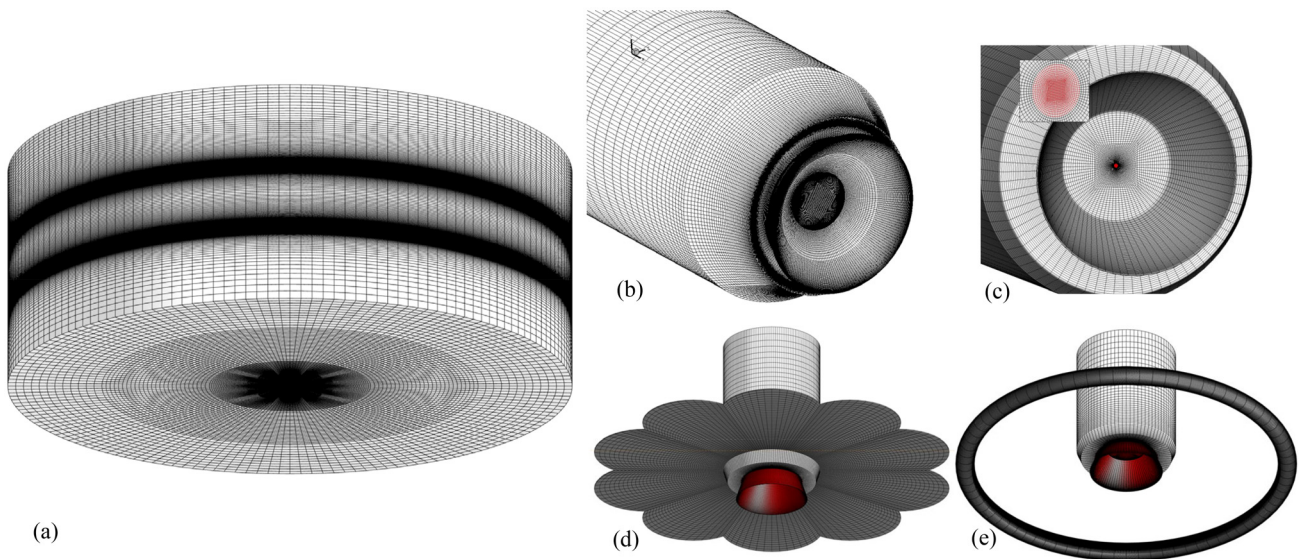
FIG. 7. Generated three-dimensional structured grid distribution over the entire computational domain (a). Close-up view of the conventional electrostatic sprayer (b) and (c), with HVRB conductor (d) and HVACR conductor (e) head surface mesh.

and 13.5×10^6, the medium grid (8.5×10^6) shows satisfactory agreement compare to available numerical and experimental results of other works. The y^+ values and prism layer height are considered 0.35 and 1.4×10^{-4} m (at solid boundaries) for the medium grid to accurately capture the high-Reynolds turbulent flow dynamic mechanisms at the

boundary layer. Also, a mesh sensitivity evaluation by considering the Kolmogorov power law-decay ($f^{-5/3}$) and proper capturing of turbulent flow details is obtained. The total number, quality, and grid distribution for two additional novel ERBSs with the HVRB and HVACR conductors were generated in a similar manner and nearly comparable
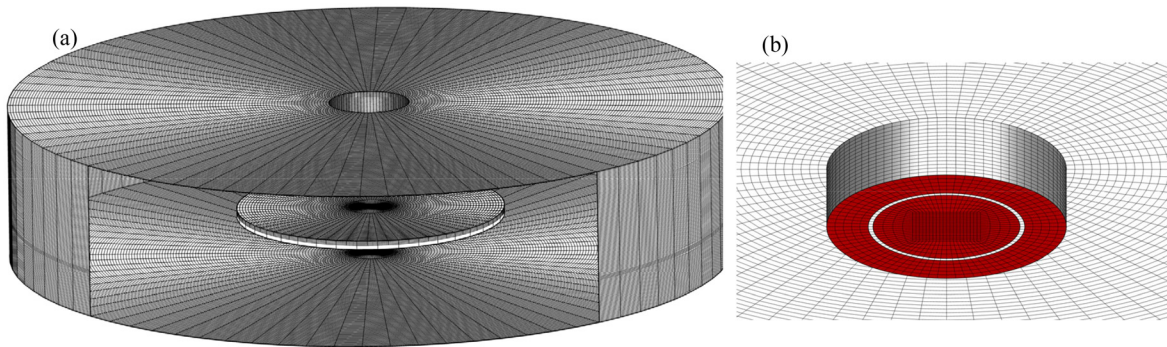
FIG. 8. Structured grid visualization around the designated geometry for the Nitrotherm spraying analysis (a). Close-up view of the injection section (b).

quantities. As an example, the overall computational cost in terms of simulation time is 774 h for the case of conventional ERBS at a voltage of −40 kV when utilizing 60 processor cores. Figure 8 shows the generated mesh for the simplified designed geometry employed for the Nitrotherm spray analysis. The mesh is produced in the same manner and quality mentioned in the previous case, with a total of 1.2×10^6 cells.

C. Validation

Before employing optimized considered computational code, its accuracy is validated, and the results are compared to the available experimental data in three various stages of spraying. In Fig. 9(a), our numerical result in the stage of the paint film propagation and spiral distribution inside the bell cup surface is compared to the experimental snapshots of Shen et al. (2019), and a suitable qualitative agreement is observed. In the next stage, the subtended angle of shaping air flow outward close to the sprayer rim is compared with the experiment of Darwish Ahmad et al. (2018) [see Fig. 9(b)]. The obtained angle by present code $\alpha = 134.76°$ is close to the experiment $\alpha = 136°$ ones. Figure 9(c) compared the sprayed

paint droplets distribution pattern of current work with the experiment distribution data of Darwish Ahmad et al. (2018), at the same operational conditions. It must be noted that an infrared thermographic flow visualization (IRFV) approach has been used in experimental reference to qualitatively evaluate the spray morphology. In brief, in this technique the thermal waves start to attenuate after traveling through the droplets, then the transmitted waves can be captured by means of the infrared camera. The acceptable capturing of radial instabilities and spray border curvature by the present numerical package is clear. Detailed information regarding the mentioned experimental work's operational setup and discussion about flow pattern can be found in the author's previous works by Pendar and Páscoa (2020).

III. RESULTS AND DISCUSSION
A. TE improvement of electrostatic spraying: Employing high-voltage conductors

Figures 10–12 evaluate the spray droplets dispersion schema, colored by their velocity, using three electrostatic sprayers of the
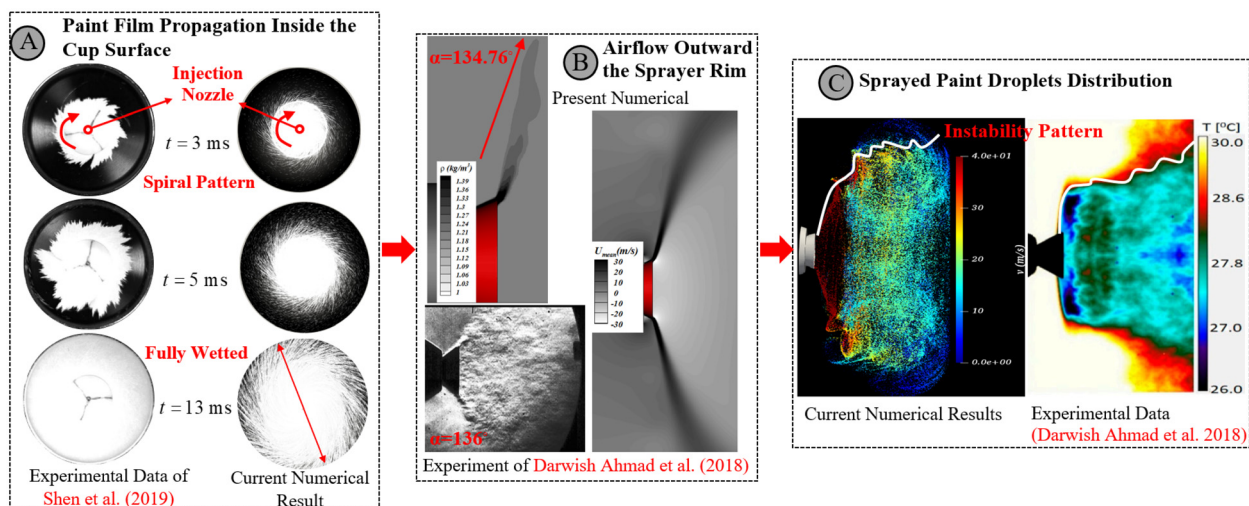

FIG. 9. The code validation by comparing the current numerical results with the experimental data: (a) Paint film propagation inside the rotary cup surface, Exp. of Shen et al. (2019) ($\omega_{bell} = 30k$ RPM, $m_{paint} = 400$ ml/min, $t = 5$, 13 ms); (b) Airflow pattern outward the sprayer cup near the rim ($\omega_{bell} = 50$ kRPM, $m_{air} = 150$ LPM, Reynolds $= 5.1 \times 10^3$), and (c) 3D sprayed paint droplets distribution, Exp. of Darwish Ahmad et al. (2018) ($\omega_{bell} = 50$kRPM, Scale Factor of Droplets $= 100$).
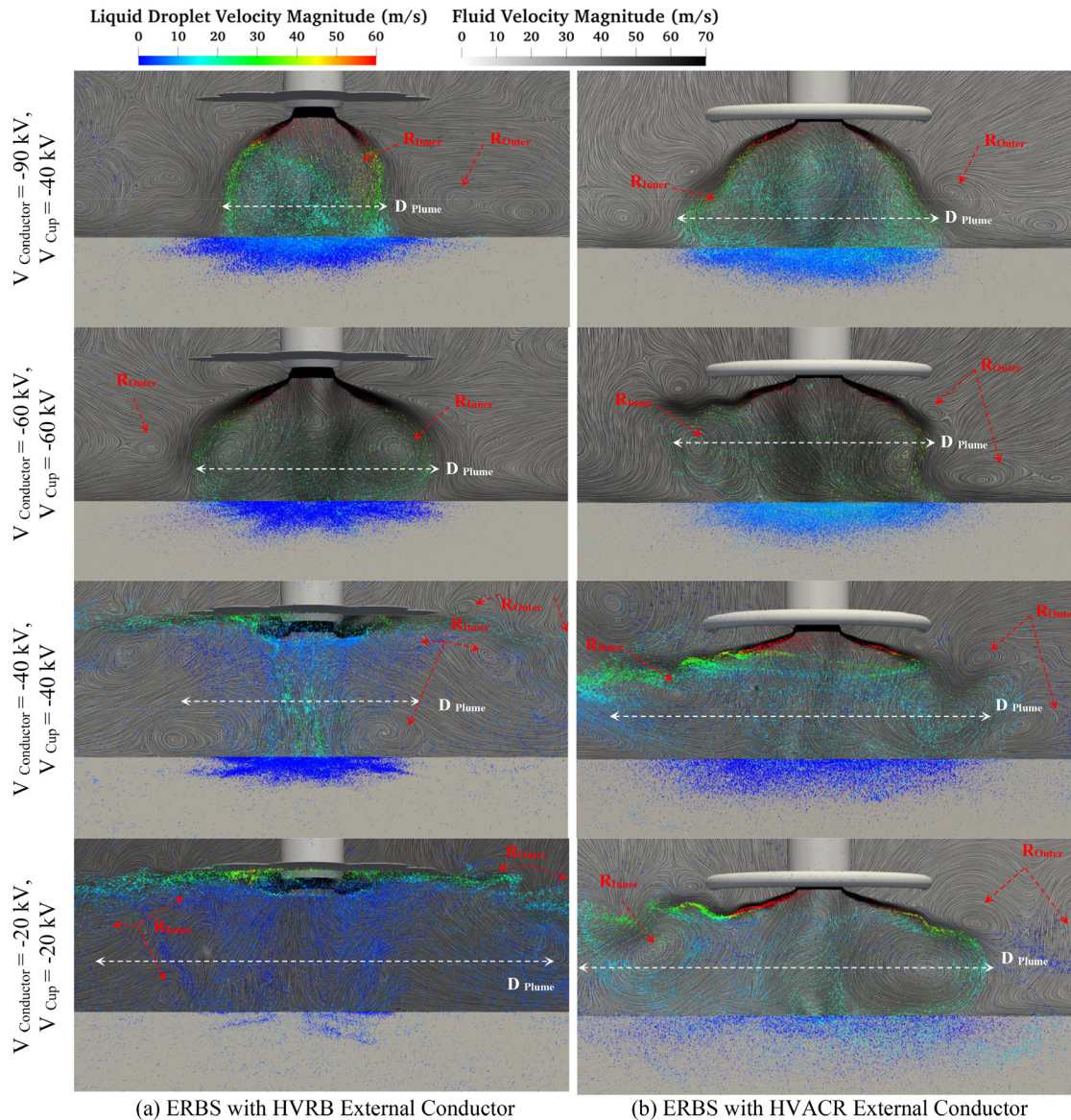
FIG. 10. 3D views of the spray droplets distribution pattern, together with the 2D center plane of velocity magnitude contour with streamline visualizing and vortical structures (using LIC method) for ERBS with (a) HVRB and (b) HVACR external conductors, evaluated a broad range of voltage applied for sprayer's body and conductors ($\omega_{Bell} = 30$kRPM, $\rho_m^q = -0.5$ mC/kg, $SF_{Droplet} = 200$, $t = 90$ms).

conventional ERBS, with the HVRB or HVACR external conductors in various operational conditions. In the background, the 2D center plane of the velocity magnitude contour with streamline visualization and vortical structures (using the LIC (Line Integral Convolution) method) is presented. In Fig. 10, four voltage ranges, from low to high, for the sprayer's cup and conductors are examined for the ERBS with the HVRB and HVACR conductors. Noticeable impacts are visible in the droplets' trajectory behavior and deviation. The nature of the manipulated/optimized electric field by adding the inventive HVRB and HVACR conductors (see Fig. 5) and consequent occurrence of

electric force interaction with the other forces cause fast/accurate movement of the atomized droplets and formation of the thicker paint film, especially in the higher negative voltage values ($\approx V \le -40$ kV). At negative voltage values higher than the mentioned specific limit ($V \le -40$ kV), a more compacted/harmonized spray plume with a narrower shoulder curve due to electric force is generated in the case with the HVRB, which shows the effectiveness of this innovative system in these operational regimes. In the lower negative voltage values, the droplets deviate to the improper transverse direction due to insufficient electric potential distribution, mostly in the case of HVRB.
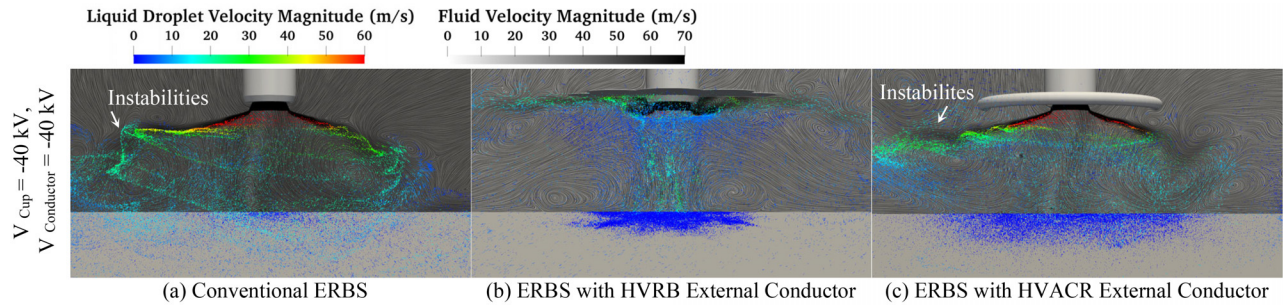
FIG. 11. Paint spray distribution comparison for three introduced electrostatic spraying systems in Fig. 2: (a) Conventional ERBS, ERBS with (b) HVRB and (c) HVACR external conductors ($\omega_{Bell} = 30$ kRPM, $\rho_m^q = -0.5$ mC/kg, $SF_{Droplet} = 200$, $t = 90$ ms). Velocity magnitude contour with streamline is visualized as a 2D-centered plane in the background.

The evolution of the circular cross section's diameter (D_{Plume}), proves a decrement in D_{Plume} by growing the negative voltage value and obtaining more coverage area in both HVRB and HVACR (see Fig. 10). As shown in Fig. 10, the formed high-speed air velocity and toroidal vortex patterns of continuous phase inside and around the spray plum among the bell cup and target, in both cases exhibit the same discipline with obvious size distinction. The time is selected when the spraying flow reaches the self-similarity condition and becomes fully characterized ($t \geq 90$ ms). The inner toroid−shape recirculation zone length (R_{Inner}) drastically reduced in higher electric potential values. In other words, the outer toroid−shape recirculation zone (R_{Outer}) forced the spray shoulder to move closer toward the axial centerline, particularly in cases using the HVACR conductor. Despite high turbulence intensity and intense vortical structure in these two designated systems

in maximum potential field distribution, the toroidal vortex structures in the continuous phase are controlled optimally. These two presented new-generation of ERBS design dramatically increase the transfer efficiency (TE), as compared in Fig. 16.

The continuous and discrete phase for three different ERBS models considered in the present work, at the moderate voltage range under identical operating conditions and simulation time, is compared in Fig. 11 and shows the efficiency and operationality of the presented pure conductors. In cases employed supplements compared to the conventional sprayer, higher electric force combined with momentum turns droplets from the recirculation flow and directs them toward the center-covered region (Fig. 11). The spray shape, instability pattern and vortex breakdown mechanisms, the same as that observed in the study by Stevenin *et al.* (2015) and Pendar and Páscoa (2020), in the
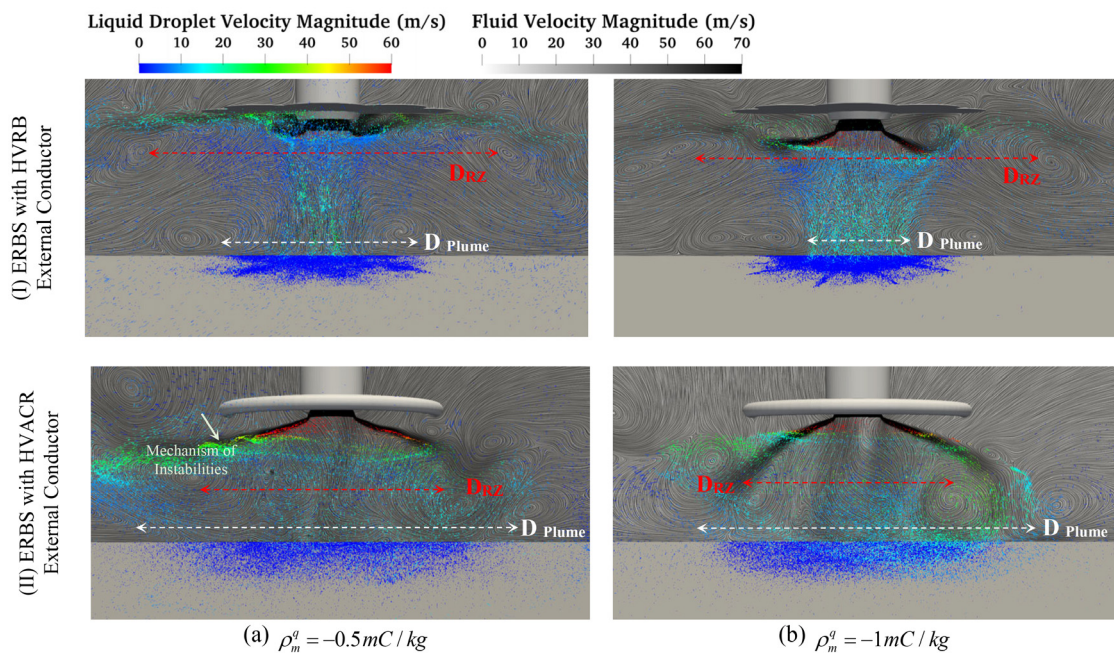
FIG. 12. Comparison of droplets path inside the formed spray plume, and streamline pattern for two various charge values (ρ_m^q) of (a) -0.5 mC/kg, and (b) -1 mC/kg ($\omega_{Bell} = 30$ kRPM, $V_{Cup} = -40$ kV, $V_{Conductor} = -40$ kV).
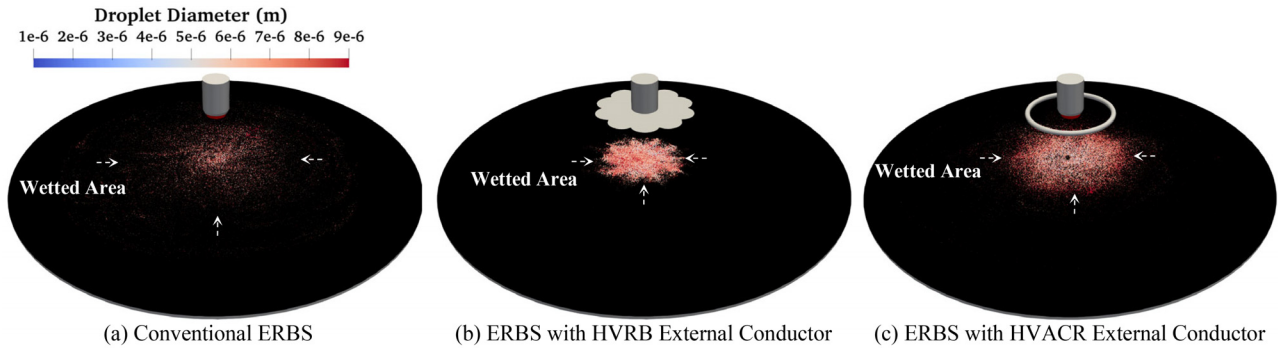
Droplet Diameter (m)
1e-6 2e-6 3e-6 4e-6 5e-6 6e-6 7e-6 8e-6 9e-6

(a) Conventional ERBS (b) ERBS with HVRB External Conductor (c) ERBS with HVACR External Conductor

FIG. 13. The deposited paint droplets pattern on the target surface for the designated sprayer systems and operational conditions were introduced in Fig. 11. (a) Conventional ERBS, (b) ERBS with HVRB external conductor, and (c) ERBS with HVACR external conductor.

plume's shoulder for the conventional ERBS [Fig. 11(a)] and the ERBS with the HVACR [Fig. 11(c)] is almost identical, but the transfer efficiency in the latter is drastically higher. In Fig. 12, the droplets charge value effect (ρ_m^q), as one of the important parameters, has been examined. These droplets proportion to their charge amount is affected by the locally produced electric field via sprayer surface and conductors. The droplets with higher charge ($\rho_m^q = -1\,\text{mC/kg}$) in the face of the electric field move toward the target in the appropriate direction at a higher velocity, forming a spray plume with a lower diameter (D_{Plume}) and considerably thicker film. More non-uniformity and irregularity in the droplet distribution and film pattern are obtained in $\rho_m^q = -1\,\text{mC/kg}$ compared to $\rho_m^q = -0.5\,\text{mC/kg}$. The structural adjustability of the HVRB and HVACR original design [described in Figs. 5(b) and 5(c)] significantly helps with precise flow control besides what is discussed in Figs. 10–12. In the HVRB conductor, the annular

retractable blades' surface areas, distance from the rotary bell's tip, and tilting angle significantly affect the electric potential and paint spray distribution and, consequently, coverage areas and uniformity. Also, pin levels in the HVACR conductor allow adjusting the ring diameter to control the spray plume size for different coating operational conditions. These two techniques enable industrial manufacturers to optimize the process and reduce material and energy consumption.

Figures 13–15 presented the wetted deposition area, droplets colored by their size, for precise evolution of the conductor coupled with the ERBS. A clear distinction in sticked droplet sizes, collision patterns on the target, coverage areas (wetted), formed film thickness and deposited film homogeneity is evident for the three presented electrostatic sprayers in Fig. 13. The efficiency of the inventive-introduced designs regarding mentioned features is proved [see Figs. 13(b), 13(c), and 14].
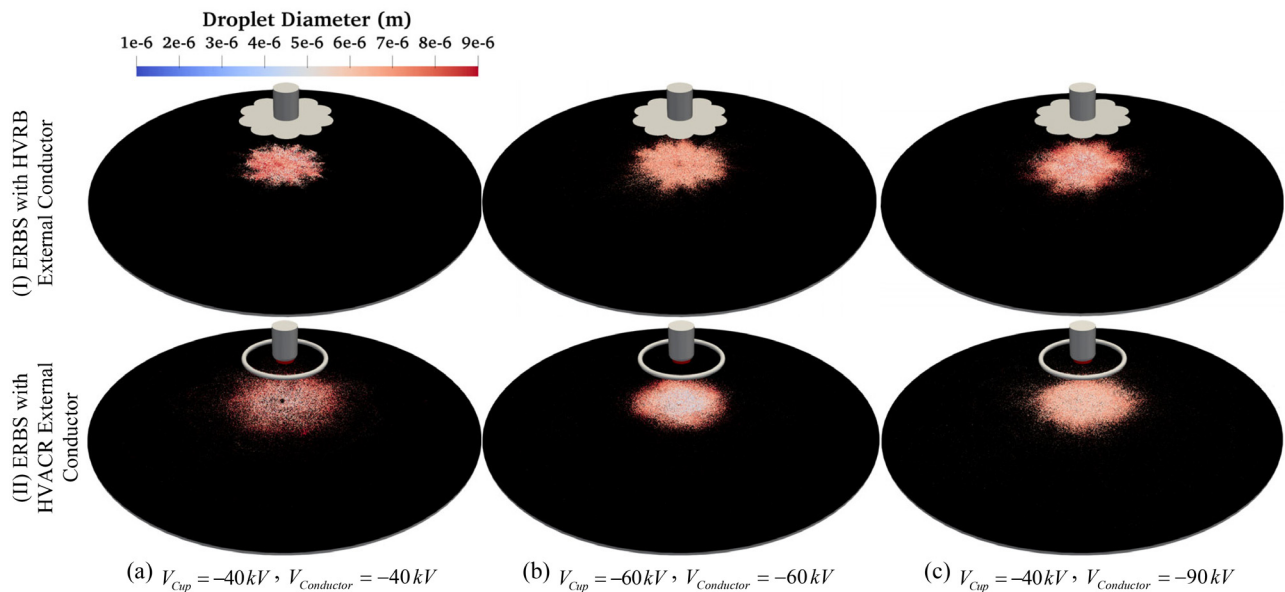

Droplet Diameter (m)
1e-6 2e-6 3e-6 4e-6 5e-6 6e-6 7e-6 8e-6 9e-6

(I) ERBS with HVRB External Conductor

(II) ERBS with HVACR External Conductor

(a) $V_{Cup} = -40\,kV$, $V_{Conductor} = -40\,kV$ (b) $V_{Cup} = -60\,kV$, $V_{Conductor} = -60\,kV$ (c) $V_{Cup} = -40\,kV$, $V_{Conductor} = -90\,kV$

FIG. 14. Illustration of stuck paint droplets on the workpiece for the ERBS with HVRB and HVACR external conductor at various voltage of (a) $V_{Cup} = -40\,\text{kV}$, $V_{Conductor} = -40\,\text{kV}$, (b) $V_{Cup} = -60\,\text{kV}$, $V_{Conductor} = -60\,\text{kV}$, and (c) $V_{Cup} = -40\,\text{kV}$, $V_{Conductor} = -90\,\text{kV}$.
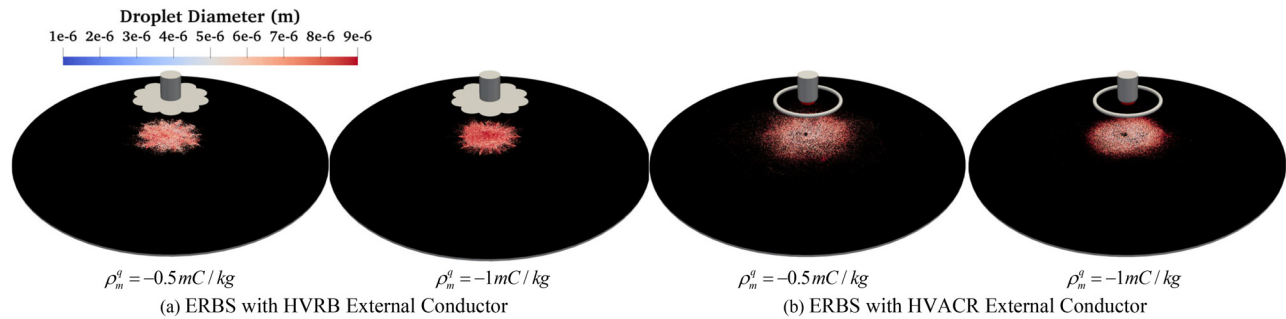
FIG. 15. Evolution of the workpiece covered area by atomized droplets considered in various charge-to-mass ratios (ρ_m^q) for the conventional ERBS equipped with (a) HVRB and (b) HVACR external conductors.

By conductor and cup surface voltage increment and subsequent influence on action force and disintegration process, resulting in a significant reduction in droplet size that allows for the formation of smooth, unblemished, esthetic appeal film (Fig. 14). The HVRB conductor is more functional than the HVACR, particularly in regimes with higher voltage values. The frames in Fig. 15 show the ERBS with the HVRB and HVACR conductors, at lower charges ($\rho_m^q = -0.5$ mC/kg), the particle sizes that covered the target are smaller than higher charges ($\rho_m^q = -1$ mC/kg). The film with higher quality, density, and prominent borders is constructed in the second operational regime.

Figure 16 presents two critical metrics for spraying process analysis, the overall transfer efficiency (TE) and Sauter mean diameter (SMD), for all considered scenarios in this section. The $TE = (m_f - m_i) \times 100/m_{out}$ is defined as a ratio of total droplet mass deposited on the goal to total what is sprayed from the sprayer. m_i, m_f, and m_{out} are the initial mass, mass after painting/drying, and the mass expelled from the sprayer nozzle. The $SMD = \sum N_i D_i^3 / \sum N_i D_i^2$ as criteria for droplet fineness is defined as a droplet diameter with an identical volume ratio to surface area for the entire spray. N_i and D_i denote the diameter of droplet and numbers in the ith size range. The comparison of the TE at the moderate (-40 kV)/low (-20 kV) regimes of voltage for the conventional electrostatic sprayer (CES) with the HVRB and HVACR conductors, show 12.21%/14.96% and 7.41%/11.82% increment compared to the CES. The TE values are significantly impacted by increasing the voltage of conductors, which shows the proposed design effectiveness and the CES with HVRB shows the best results. The highest TE of 85.15% and 80.78% are obtained in the voltage conductor's maximum values for the HVRB and HVACR conductors. Also, in the high droplets charge ($\rho_m^q = -1$ mC/kg) these values increase to 85.67% and 82.78%, respectively [see Fig. 16(a)].

The average SMD sizes prove appropriate disintegration for obtaining fine film by using the CES with the HVRB and HVACR conductors compared to the CES. The moderate (-40 kV)/low (-20 kV) voltage operation regimes for the ERBS with the HVRB and HVACR conductors, show 3.0%/0.98% and 8.7%/1.1% decrement in average SMD compared to the CES. Yet/However, the average SMD size at the peak of the voltage (-90 kV) for the conductor, the HVRB obtained 5.94% growth compared to the HVACR. In sum, the HVRB and HVACR show the best performance concerning the disintegration process and spray size distribution for the average and high voltage ranges.

B. TE improvement of electrostatic spraying: Applying nitrotherm spray technique

Here the employment of a novel Nitrotherm spraying method during the electrostatic coating for geometry described in Fig. 3 is investigated. Using this method improves the application time to reach faster drying time, higher film quality, less material consumption, lower contamination in the booths, higher transfer efficiency. Here, the effect of prominent parameters of the injected nitrogen velocity (Fig. 17), sprayed droplets size distribution (Fig. 18), injected nitrogen temperature (Fig. 19), sprayed droplets charge-to-mass ratios (ρ_m^q) (Fig. 20), and the voltage of body surface (Fig. 21) on the Nitrotherm spraying process is analyzed over a broad range. Cahnging of the mentioned variations significantly affect on the spraying and deposition process. As the following results prove, the mentioned prominent parameters significantly affect the spraying and deposition pattern.

Figure 17 depicts the injected heated nitrogen velocity effect by the evolution of the vortical structures with velocity magnitude contours (I) and sprayed paint droplets deposited pattern (II). As is visible, the injected nitrogen velocity significantly affects the droplet's deviation, overspray phenomenon, covered areas borders irregularity, film thickness, and central filling. The five mentioned meaningful items are optimized by growing the nitrogen injection velocity, and denser and thicker finishes with high TE are produced.

Strike a balance between particle size, as the dominant influencing parameters, and other metric parameters, such as injected nitrogen characteristic, is crucial. The considered sizes (minimum D_{Min}, maximum D_{Max}, and average $D_{Average}$) give to the Rosin–Rammler method as an input variable. According to Fig. 18, the wetted area resulting from the improper force interaction produced irregular and tiny areas as a consequence of decreasing size ($D_{Average} = 15 \, \mu$m). The evolution reveals that the more significant droplet size distribution obtained harmonized and thick coverage region. The diameter of the predicted deposited area gradually increased by the increment of the assumed initial droplet size, with a regular and uniform pattern.

The pure nitrogen that is separated from the air and heated for the acceleration of the evaporation times is expelled from the ring around the droplets injection nozzle. The heated nitrogen is combined with ionized droplets and the electric field. In real operation, a nitrogen generator can easily assemble to the system of the ERBS. In Fig. 19, comparing compressed, heated nitrogen (I) to compressed air (II) reveals that the former enhanced the TE and produced a more
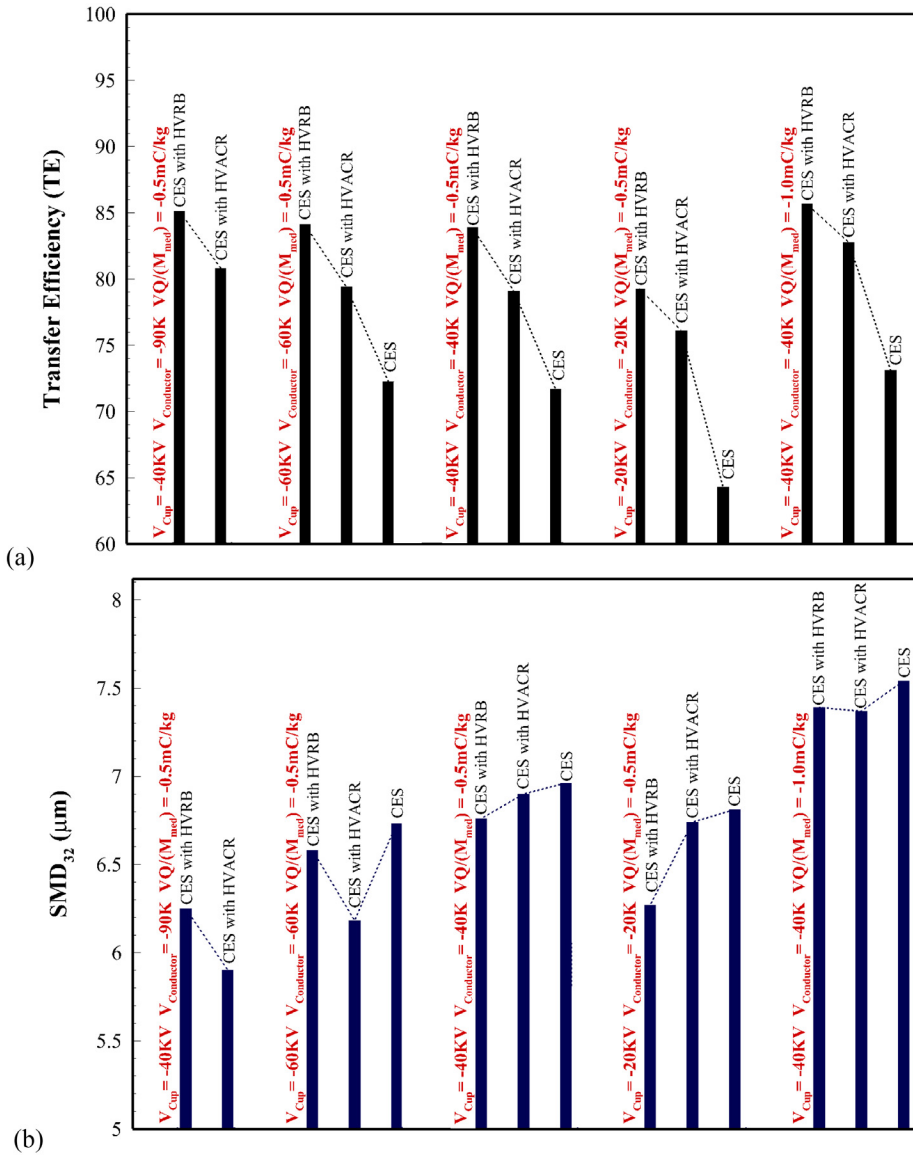
FIG. 16. The obtained values of the overall transfer efficiency (TE) (a) and Sauter-mean-diameter (SMD) (b) for the introduced cases at various operational conditions.

centralized, cosmetic, denser, and thicker film. The temperature increments of nitrogen do not significantly affect the trajectory and deposition pattern in the moderate temperature range ($T_{Nitrogen} = 343.15°K$). However, in very high temperatures, the central parts of the covered area are deposited with a smaller size range of droplets that clarify the efficiency of the Nitrotherm spraying.

Figures 20 and 21 assessed the effects of the charge-to-mass ratios (ρ_m^q) and surface voltage as key factors of electric field consideration during the Nitrotherm electrostatic spraying. These two parameters have almost the same impact on the discrete flow. Establishing a balance between the spray TE and quality by manipulating these variations and energy/material consumptions should be considered. Spray with a narrower shoulder, lower unfavorable overspray and uniform/dense deposition obtained in higher values of voltage and charge.

When the electric field is deactivated, an irregular and thin pattern is obtained. It is visible that in the moderate range of voltage and charge ($\rho_m^q = 2\,mC/kg$, $V = 60\,kV$) with optimum cost the harmonized/thicker film and denser finished surface are obtained (see Fig. 20). It can be understood that the combination of the Nitrotherm continuous phase and moderate electric field dramatically improves the behavior of the discrete spray phase.

C. Integration of deep learning models with CFD database

In this section, we describe the performance of different machine learning (ML) models for the prediction of droplet deposition and the produced film deposition pattern on the target. The model also
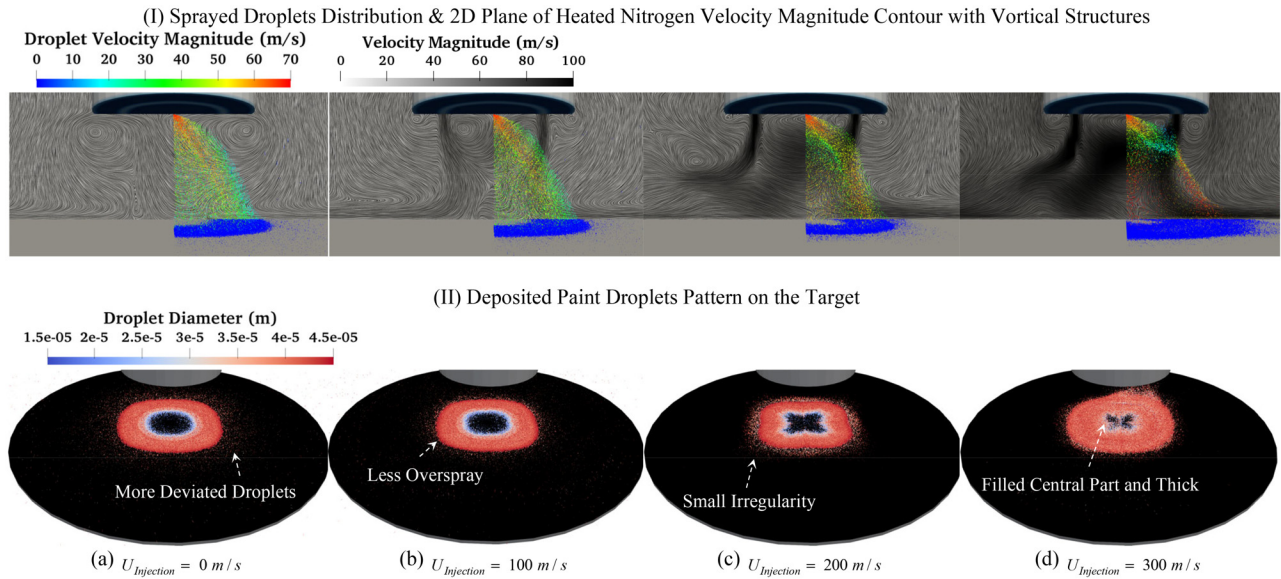
FIG. 17. Evolution of injected heated nitrogen velocity effect on the droplets trajectory and deposition pattern: (a) $U_{Injection} = 0\,\text{m/s}$, (b) $U_{Injection} = 100\,\text{m/s}$, (c) $U_{Injection} = 200\,\text{m/s}$, and (d) $U_{Injection} = 300\,\text{m/s}$ ($T_{Nitrogen} = 393.15°\text{K}$). (I) Sprayed droplets distribution and 2D plane of heated nitrogen velocity magnitude contour with vortical structures. (II) Deposited paint droplets pattern on the target.

predicts the velocity field of the Eulerian phase. This subsection aims to achieve accurate predictions with the fewest possible time steps, reducing the computational time/cost required for CFD calculations.

Our proposed Deep Learning (DL) model follows an offline approach for training, validation, and testing. In this method, the full database in analysis, in our case related to heated nitrogen, is first computed using CFD. The data generated by these CFD simulations are then fed into the ML models for training. This methodology allows us to comprehensively simulate various scenarios, capture the results, and use these data to train the DL model about the behavior of heated nitrogen. By training offline, we can efficiently ensure that a wide variety of working conditions are covered in the training data. The training of all the ML models is performed utilizing an NVIDIA Quadro P500 GPU, which offers powerful computing capability in ML problems.

1. Models' architecture

First, it must be mentioned that a total number of time steps $N = 120$ was extracted for all the simulations. Since the total time of simulation is $T = 30\,\text{ms}$, we have an extraction of snapshots with a
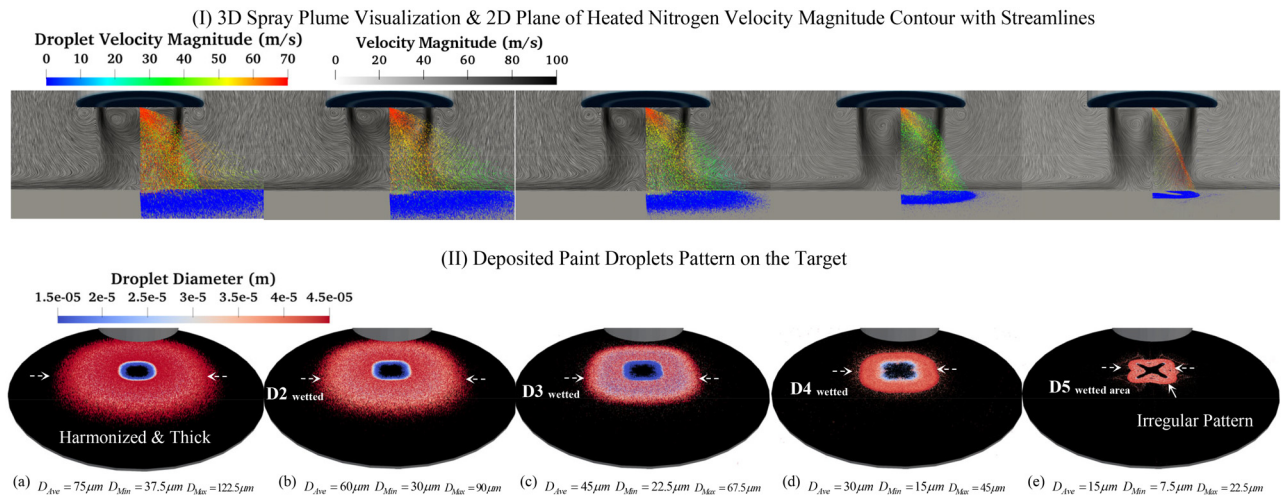

FIG. 18. Assessment of droplet size distribution impact on the droplets path and deposited film structure during the Nitrotherm electrostatic spraying process: (a) $D_{Average} = 75\,\mu\text{m}$, (b) $D_{Average} = 60\,\mu\text{m}$, (c) $D_{Average} = 45\,\mu\text{m}$, (d) $D_{Average} = 30\,\mu\text{m}$, and (e) $D_{Average} = 15\,\mu\text{m}$ ($T_{Nitrogen} = 393.15°K$). (I) 3D spray plume visualization and 2D plane of heated nitrogen velocity magnitude contour with streamlines. (II) Deposited paint droplets pattern on the target.
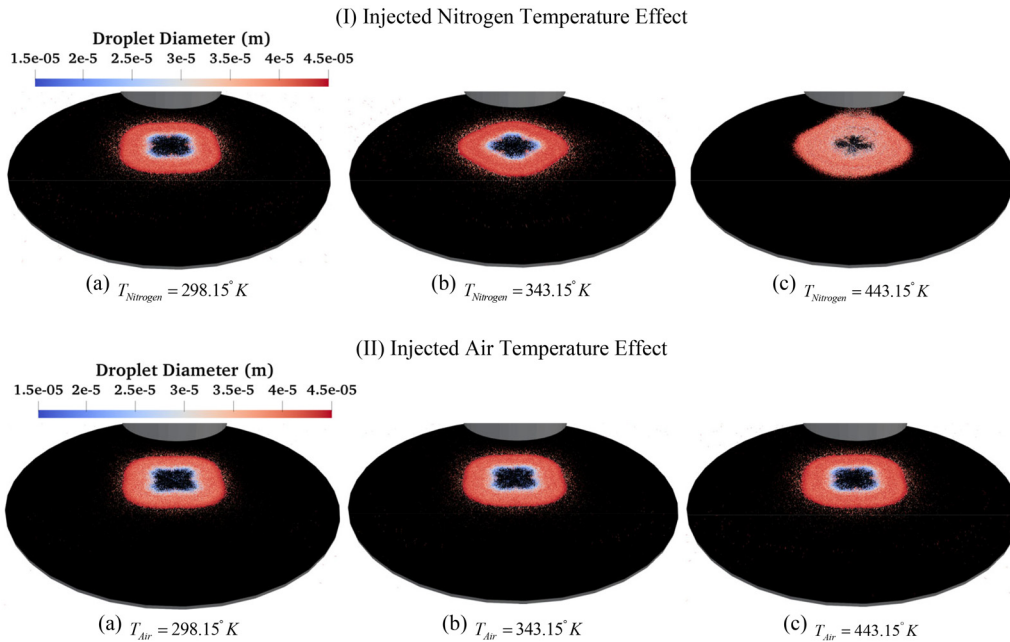
(I) Injected Nitrogen Temperature Effect

(a) $T_{Nitrogen} = 298.15°K$ (b) $T_{Nitrogen} = 343.15°K$ (c) $T_{Nitrogen} = 443.15°K$

(II) Injected Air Temperature Effect

(a) $T_{Air} = 298.15°K$ (b) $T_{Air} = 343.15°K$ (c) $T_{Air} = 443.15°K$

FIG. 19. Comparison of heated nitrogen (I) and air (II) injection impact on the droplets trajectory and deposition pattern: (a) $T = 298.15$, (b) $T = 343.15$, and (c) $T = 443.15°$K. (I) Injected nitrogen temperature effect. (ii) Injected air temperature effect.

time step of $\delta t = 0.25$ ms. The initial goal is to find a suitable model that has input N_s snapshots of the side view of the spray, of the times $t : \{t_1, t_2, \ldots, t_{N_s}\}$ which can give a prediction of the final spray deposition. This output is given by an image snapshot of the top view of the plate target at the time $t = t_f$, which shows the density of the deposited droplets. The parameter conditions define various test cases $\{T_{N_2}, U_{N_2}, V, D_d, q/m\}$. The last two values are the emitted droplets' size and the electric charge-to-mass ratio. These two can be joined, defining the maximum droplet size, and so, the working condition of a specific case becomes $W_s : \{T_{N_2}, U_{N_2}, V, D_{max}\}$. Reducing the
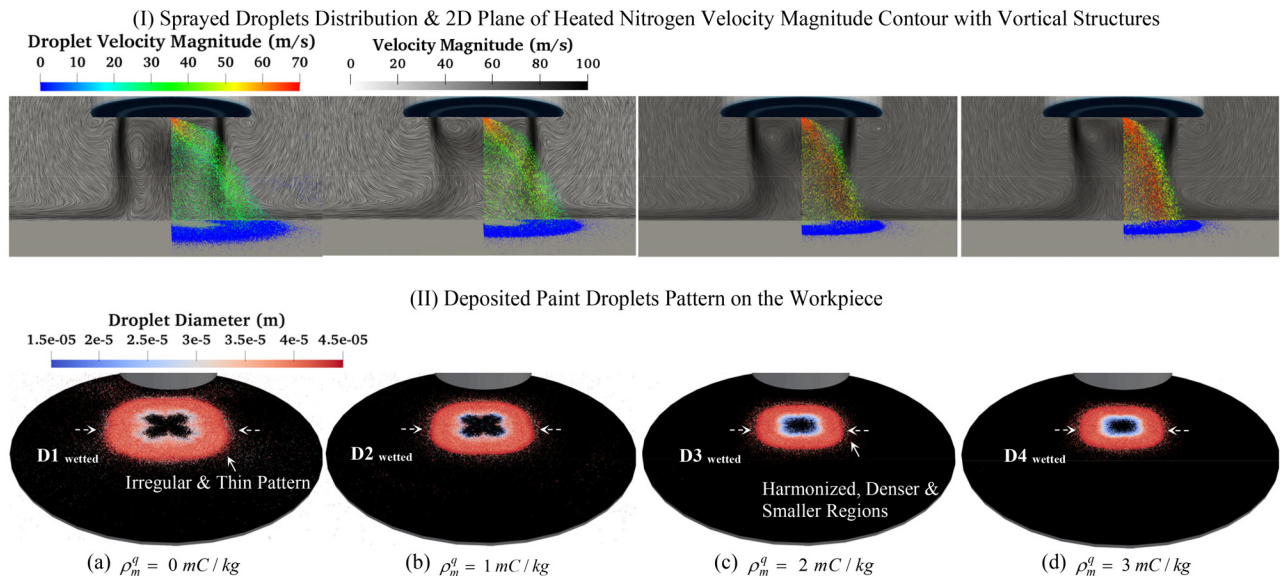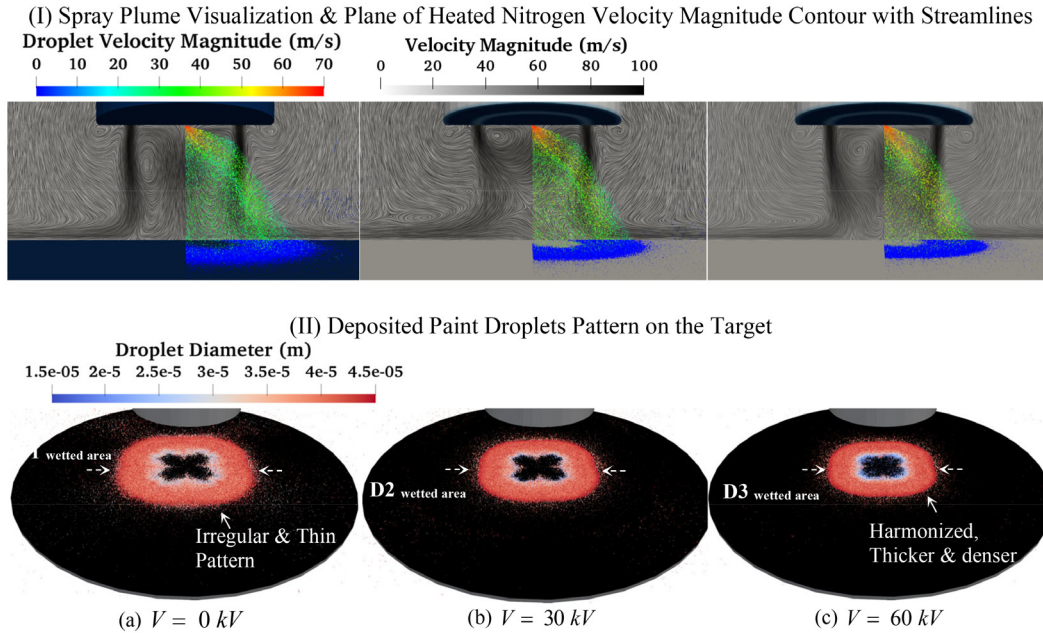
(I) Sprayed Droplets Distribution & 2D Plane of Heated Nitrogen Velocity Magnitude Contour with Vortical Structures

(II) Deposited Paint Droplets Pattern on the Workpiece

(a) $\rho_m^q = 0\ mC/kg$ (b) $\rho_m^q = 1\ mC/kg$ (c) $\rho_m^q = 2\ mC/kg$ (d) $\rho_m^q = 3\ mC/kg$

FIG. 20. Examination of the charge-to-mass ratios (ρ_m^q) influence during the Nitrotherm electrostatic spraying process: (a) $\rho_m^q = 0\ mC/kg$, (b) $\rho_m^q = 1\ mC/kg$, (c) $\rho_m^q = 2\ mC/kg$, and (d) $\rho_m^q = 3\ mC/kg$ ($T_{Nitrogen} = 393.15°$K). (I) Sprayed droplets distribution and 2D plane of heated nitrogen velocity magnitude contour with vortical structures. (II) Deposited paint droplets pattern on the workpiece.

FIG. 21. Evolution of various body surface voltage effect on the droplets trajectory and deposition shape during the Nitrotherm electrostatic spraying: (a) $V = 0$,(b) $V = 30$, and (c) $V = 60$ kV($T_{\text{Nitrogen}} = 393.15°$K). (I) Spray plume visualization and plane of heated nitrogen velocity magnitude contour with steamlines and (II) deposited paint droplets pattern on the target.

number of parameters that characterize a case helps with the correlations for the machine learning model.

Different machine learning (ML) model architectures were tested in this study, and different hyperparameters were set for each one. To obtain an optimized model, the results with various hyperparameters are compared. The evaluated models were built using the Convolutional Auto-Encoder (CAE) architecture, which employs two Convolutional Neural Networks (CNN), one for encoding and another for decoding. The core of the design is depicted in Fig. 22, and several models differ in the type of layers employed but not in the structure.

The core of a CNN is its convolutional layer, which extracts features from the input data through a user-defined filter. The output of a convolutional layer can be calculated using the following equation (Mondal and Sarkar, 2022):

$$y_{i,j,k} = f\left(\sum_{a=1}^{m}\sum_{b=1}^{n}\sum_{c=1}^{d} w_{a,b,c,k}x_{i+a-1,j+b-1,c} + b_k\right), \quad (19)$$

where $y_{i,j,k}$ is the output of the kth feature map at position (i,j), f is the activation function, $w_{a,b,c,k}$ is the weight of the kth filter at position (a,b,c), $x_{i,j,c}$ is the input pixel value at position (i,j) and channel c, and b_k is the bias term for the kth feature map. The initial proposed autoencoder is composed of the layers of Table II. Each convolutional/deconvolutional layer was followed by a batch normalization layer and a rectified linear unit (ReLU) activation function. We define the model architecture by the size of the filters of encoding/decoding (N_1, N_2, N_3) and fully connected layers (N_L) neurons number. Table II proposes the $8 \times 16 \times 32$ (64) architecture, a model called initial CAE model used to observe the filter size increasing effect.

The encoding and decoding CNNs are connected with a flattened latent space. This space is connected by a concatenate layer with the working condition array W_s for increasing the awareness of the model to the physical condition of the images. Since our input is temporal images, we add a recurrent layer on the latent space. This type of layer is called allow information to be passed from time step to time step. This is the case of Long Short-Term Memory (LSTM) which creates a loop that allows the network to maintain an internal state, which can capture the temporal dependencies in the data. The output of an LSTM layer at time step t can be calculated using the following equations (Deng et al., 2019):

$$f_t = \sigma\left(W_f x_t + U_f h_{t-1} + b_f\right), \quad (20)$$

$$i_t = \sigma(W_i x_t + U_i h_{t-1} + b_i), \quad (21)$$

$$o_t = \sigma(W_o x_t + U_o h_{t-1} + b_o), \quad (22)$$

$$c_t = f_t \odot c_{t-1} + i_t \odot \tanh(W_c x_t + U_c h_{t-1} + b_c), \quad (23)$$

$$h_t = o_t \odot \tanh(c_t), \quad (24)$$

where σ is the sigmoid activation function, $\odot$ is the element-wise multiplication operator (or Hadamard product), x_t is the input at time step y_i, h_{t-1} is the output of the previous time step, c_t is the cell state, and f_t, i_t, o_t are forget, input, and output gates, respectively. The "forget" gate means that the cell status can be "forgotten" if the gate it's on. This type of cell can be combined with the convolutional layers, gaining then the capability of handle spatial-temporal patterns calls ConLSTM layers (Shi et al., 2015; Gao et al., 2022). We created a model called CAE_LSTM, which has the same architecture $8 \times 16 \times 32(64)$, but the convolution layers are replaced by ConLSTM and the Max-Pooling becomes three-dimensional (3D), which as a kernel of (1, 2, 2).
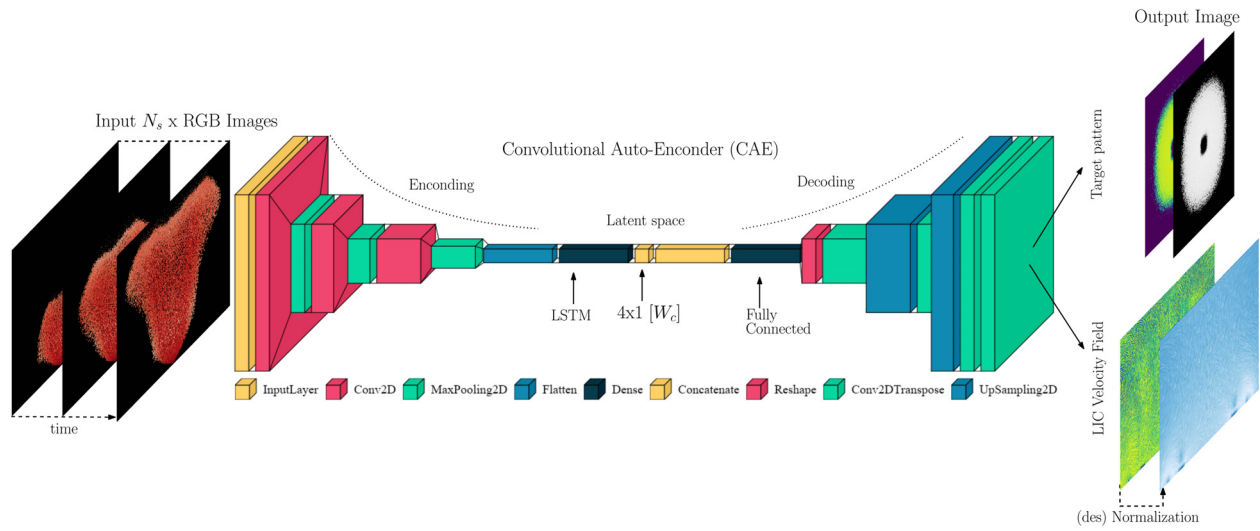
FIG. 22. Schematics of the proposed Convolutional Auto-Encoder (CAE) architecture.

TABLE II. Proposed architecture of the $8 \times 16 \times 32(64)$ Convolutional Auto-Encoder (CAE) model.

| Layer	Layer Type	Kernel, Output dim.	Kernel size	No. filters/neurons
		Encoder		
0	Input	(Ns, 512, 512, 1)	$\cdots$	$\cdots$
1	Convolution	(Ns, 512, 512, 8)	(3, 3)	8
2	Max-Pooling	(Ns, 256, 256, 8)	(2, 2)	$\cdots$
3	Convolution	(Ns, 256, 256, 16)	(3, 3)	16
4	Max-Pooling	(Ns, 128, 128, 16)	(2, 2)	$\cdots$
5	Convolution	(Ns, 128, 128, 32)	(3, 3)	32
6	Max-Pooling	(Ns, 64, 64, 32)	(2, 2)	$\cdots$
7	Convolution	(Ns, 262144)	(3, 3)	64
		Fully Connected Latent Space		
8	LSTM	(Ns, 64)	$\cdots$	/64
9	Input (Ws)	(4, 1)	$\cdots$	$\cdots$
10	Concatenate	$(64 + 4)$	$\cdots$	$\cdots$
11	Fully connected	$(64 \times 64 \times 16)$	$\cdots$	/65 536
		Decoder		
12	Transpose Convolution	(64, 64, 32)	(3, 3)	32
13	Up-sampling	(128, 128, 32)	(2, 2)	$\cdots$
14	Transpose Convolution	(128, 128, 16)	(3, 3)	16
15	Up-sampling	(256, 256, 16)	(2, 2)	$\cdots$
16	Transpose Convolution	(256, 256, 8)	(3, 3)	8
17	Up-sampling	(512, 512, 8)	(2, 2)	$\cdots$
18	Transpose Convolution	(512, 512, 1)	(3, 3)	1
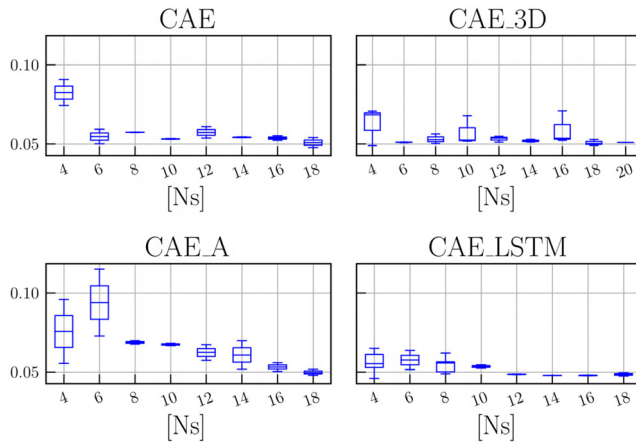
FIG. 23. Influence of the number of input snapshots (Ns) on the MSE, for different ML models tested.

Another way to capture the temporal correlations on the input images is by treating the time as a third dimension and use a 3D convolution layer (Con3D). The Con3D operation can be expressed using the following equation (Gao *et al.*, 2022; Yousif *et al.*, 2023):

$$y_{i,j,k,d} = \sum_{a=1}^{m} \sum_{b=1}^{n} \sum_{c=1}^{p} \sum_{e=1}^{q} \sum_{f=1}^{r} w_{a,b,c,e,f,d} x_{i+a-1,j+b-1,k+c-1,e,f} + b_d,$$

(25)

where $y_{i,j,k,d}$ is the output at position (i,j,k) and channel d, $w_{a,b,c,e,f,d}$ is the weight of the dth filter at position (a,b,c,e,f), $x_{i,j,k,e,f}$ is the input volume. Here, we employed these layers called CAE_3D, which used Con3D layers with a kernel size of $(3, 3, 3)$.

2. Prediction of droplets deposition on the target

The auto-encoder was trained using the mean squared error loss function and the Adam optimizer (Kingma and Ba, 2014) with a learning rate of 0.001. The performance of the model was monitored on the validation set using the Mean Squared Error (MSE) and Mean Absolute Error (MAE) metrics that are defined as

$$L_{MSE} = \frac{1}{n} \sum_{i=1}^{n} (y_i - \hat{y}_i)^2,$$

(26)

$$L_{MAE} = \frac{1}{n} \sum_{i=1}^{n} |y_i - \hat{y}_i|,$$

(27)

where n is the number of samples, y_i and $\hat{y}_i$ are the true and predicted values of the ith sample. The data were divided in (N_t, N_v, N_{te}) = (21, 3, 2), corresponding to the number of cases for training, validation and for testing, respectively. Since our dataset is composed of a small dataset (26 cases), the validation/training was 13%, and the convergence of the models upon the epoch was defined by an early stopping criterion, avoiding overfitting the model's parameters. This criterion stops the training whenever the L_{MSE} error is bigger than the minimum reached within 1000 epochs.

The two cases for testing the predictions of the model are defined as follows:

Test A, W_s : $\{393.15\,\text{K}, 150\,\text{m/s}, 30\,\text{kV}, 5.72 \times 10^{-4}\,\text{nm}\}$ and Test B, W_s : $\{393.15\,\text{K}, 150\,\text{m/s}, 60\,\text{kV}, 45.8 \times 10^{-4}\,\text{nm}\}$. These two test cases are not fed to the DL training or validating procedure, so they are unseen by the model in the training step and just used in the testing step to ensure a generalization. These testing cases are highlighted in Fig. 4. Figure 23 shows the significant role of the snapshot numbers [Ns] as an input for the DL model. Here, we observed the MSE loss parameter. The outcome reveals a distinctive influence on the MSE reduction for the CAE and CAE_LSTM model.
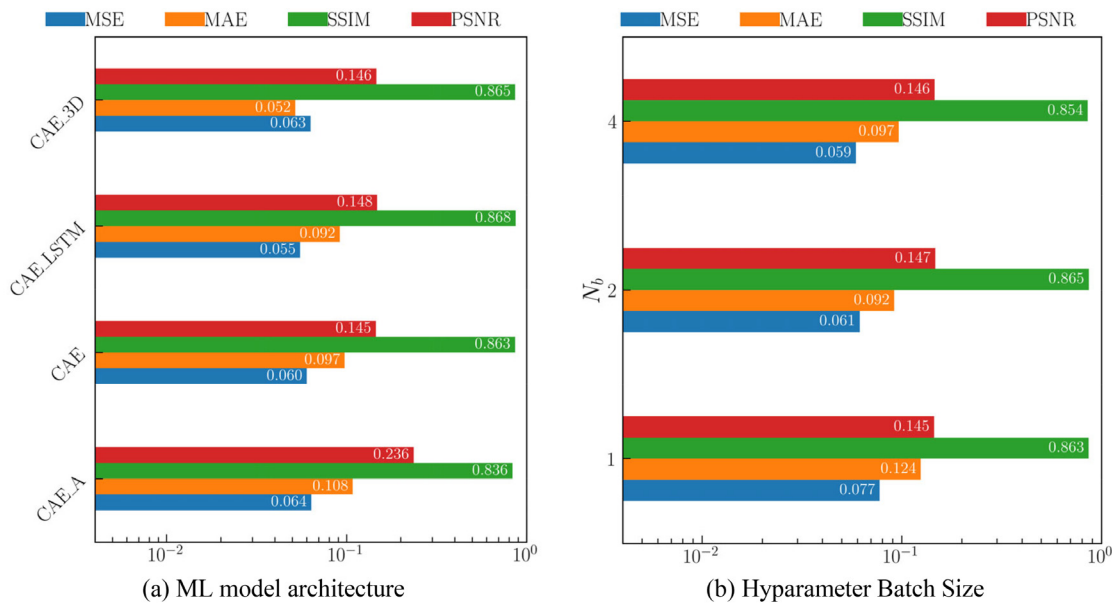

FIG. 24. Influence of the (a) model architecture and (b) the hyper parameter batch size (N_b). Accuracy parameters calculated for the validation test cases.

This pattern signifies a convergence in the MSE, indicating that the error tends to stabilize once a certain threshold of Ns is given. Specifically, a steady-state performance is achieved at approximately 12 snapshots for the CAE_LSTM model, suggesting that further increasing the input size does not substantially enhance model accuracy. It also underscores the interplay between deep learning architectures and the dynamic temporal dependencies within the data, which is very well captured by the CAE_A and CAE_LSTM. Considering a batch size of 1, 2, and 4, we tested for the different models designed [Fig. 24(a)] and for different sizes of input snapshots [Fig. 24(b)]. The quantitative comparison between the model architectures, the choice of the input snapshot number, and the hyperparameters for choosing the best ones are initially made with the MSE and MAE errors.

Since we are dealing with images, two more common parameters in this field are used to ensure the reconstruction quality of the images.

The first is the Structural Similarity Index (SSIM), a metric used to measure the similarity between two images, $\text{SSIM}(x, y) = \frac{(2\mu_x\mu_y + c_1)(2\sigma_{xy} + c_2)}{(\mu_x^2 + \mu_y^2 + c_1)(\sigma_x^2 + \sigma_y^2 + c_2)}$, where x and y are the two images being compared. A higher SSIM value indicates a greater similarity between the images. The other important measurement is the Peak Signal-to-Noise Ratio (PSNR) given by $\text{PSNR} = 10 \cdot \log_{10}\left(\frac{\text{MAX}^2}{\text{MSE}}\right)$, where MAX is the maximum possible pixel value (e.g., 255 for 8-bit images), and MSE is the mean squared error between the original and reconstructed images.

Batch size is a crucial hyperparameter in deep learning models that regulates how many samples are sent into the machine learning model simultaneously during each training iteration. Since it can affect model convergence, generalization, and computational efficiency,
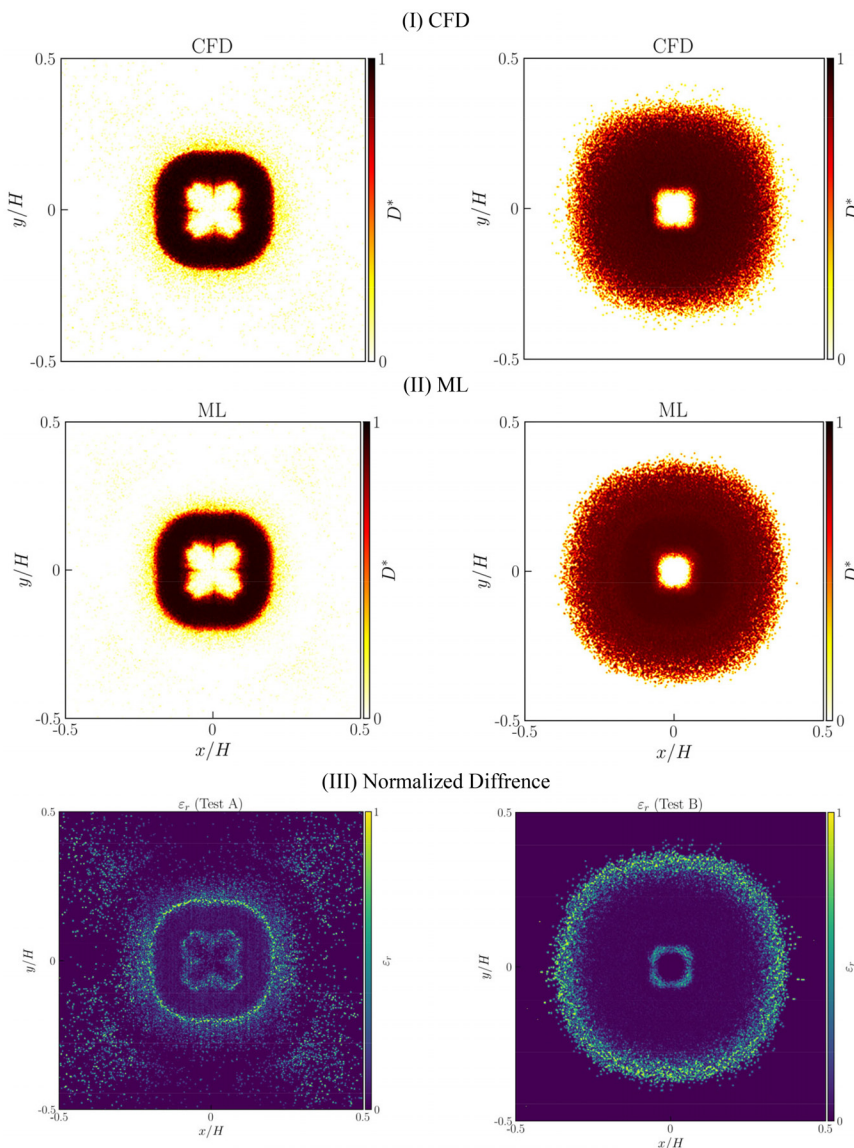

FIG. 25. Comparison of the prediction target droplet deposition. Scaled by the density D. (I) CFD, (II) ML, and (III) normalized difference.

choosing a suitable batch size is crucial in deep learning applications. The choice of batch size is typically influenced by the model's complexity, the dataset's size, the hardware's memory capabilities, and the optimization strategy used for training. Although larger batch sizes may result in faster convergence and less generalization error, they also need more memory and may cause unstable convergence. In our case, we tested for small batch sizes because two-dimensional and three-dimensional layers require a large amount of memory. The impact on the accuracy of the predictions with batch sizes of 1, 2, and 4 are shown in Fig. 24(b). In this frame, four parameters that can provide the accuracy of the prediction are calculated. This was calculated for both test cases (Test A, Test B), and the mean value was obtained. We observed that a batch size of 2 is the best, the one is too sparcy, and the four can lead to overfitting due to the small database.

With these assessments, we choose the model CAE_LSTM, with a number of input snapshots of 12 and a batch size of 2. With the model trained, we predict the droplet deposition for Tests A and B (see Fig. 25). The figure compares the CFD results (I) with the predictions made with the ML model (II). Notice that we choose two very different working conditions to truly test the generalization. The results show a very good prediction, where the core and shape are precisely captured, and the error is on the edges. For Test A, we also noticed the error on the droplets scattered by the velocity field, although what really is essential to capture is the core, which is the region of high density.

Since the goal is to predict the area of deposited droplets on the target, we calculate the final error of accuracy by the area of droplets of the CFD vs the ML prediction, being $\epsilon_A = |A_{ML} - A_{CFD}|/A_{CFD}$ (III). With this, the prediction error for the deposited droplets on the target for Test A and B are 0.877% and 0.295%, respectively. These very low errors for deposition are very promising for fast simulation of these types of fluid dynamic problems.

3. Prediction of continuous velocity field

Here, a new approach using the latest ML model is employed for predicting the continuous velocity field. This continuous velocity field is characterized by the LIC method, which enables us to identify the vortical structure's location and behavior. Here, we have implemented the same machine learning architectures and cases (Test A and Test B) as used for droplet deposition (see Fig. 26). The 2D snapshots were normalized by the distance H, which is the distance from the inlet to the plate, where $z/H = 0$ is the target wall. Moreover, the velocity field for a better comparison is normalized to $u^* = u/150$. As we observe, the predictions show very good agreement with the CFD solution. The red lines on the figures are the distances between the vortex centers, for which the prediction shows exactly the same pattern as the vortices calculated by the CFD.

As for the spray deposition pattern, we also calculated the four accuracy measurements of the image reconstruction $\{L_{MSE}, L_{MAE}, SSIM, PSNR\} = \{0.0065, 0.0194, 0.946, 0.161\}$. To check the accuracy of the field values prediction, we plot a histogram of the pixel intensity for each pixel of the predicted images and compare it with the CFD results. We tested this for the CAE and CAE_LSTM architecture, see Fig. 27.

The intensity of pixels in the reconstructed image is closely related to the velocity magnitude of the 2D plane snapshot, and
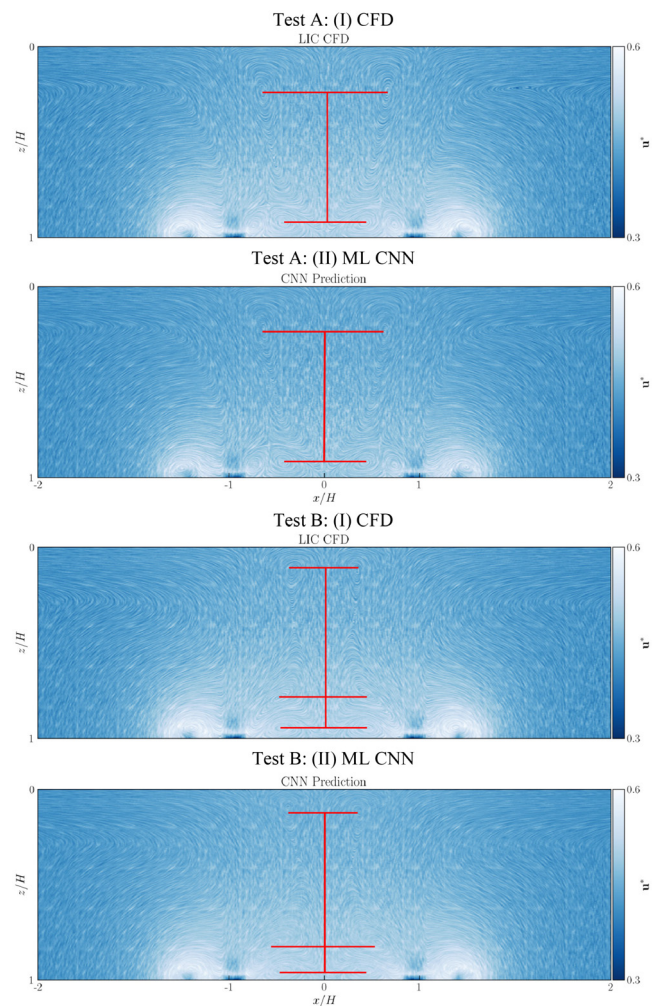
FIG. 26. Comparison of the continuous velocity field predicted results with CFD data for both test cases. Test A: (I) CFD Test A: (II) ML CNN Test B: (I) CFD Test B: (II) ML CNN.

therefore, the area of the pixel intensity histogram can be used as an indicator of the flow energy. By analyzing this relationship, we can evaluate the performance of the two different deep learning models for this specific prediction task. Our results demonstrate that the CAE_LSTM model outperforms the simple CAE model for predicting the LIC. As we observed in our analysis of droplet target prediction, incorporating cells that are aware of temporal dynamics significantly enhances prediction accuracy.

IV. CONCLUSION

The present study conducted a comprehensive hybrid analysis of high-fidelity CFD and deep learning (DL) for maximizing the electrostatic spraying process efficiency. The results prove that employing designed novel conductors with high-voltage retractable blades (HVRB) and high-voltage adjustable control-ring (HVACR) in combination with Nitrotherm spraying technique during the electrostatic atomizing allows the spraying industrial manufacturers to reduce
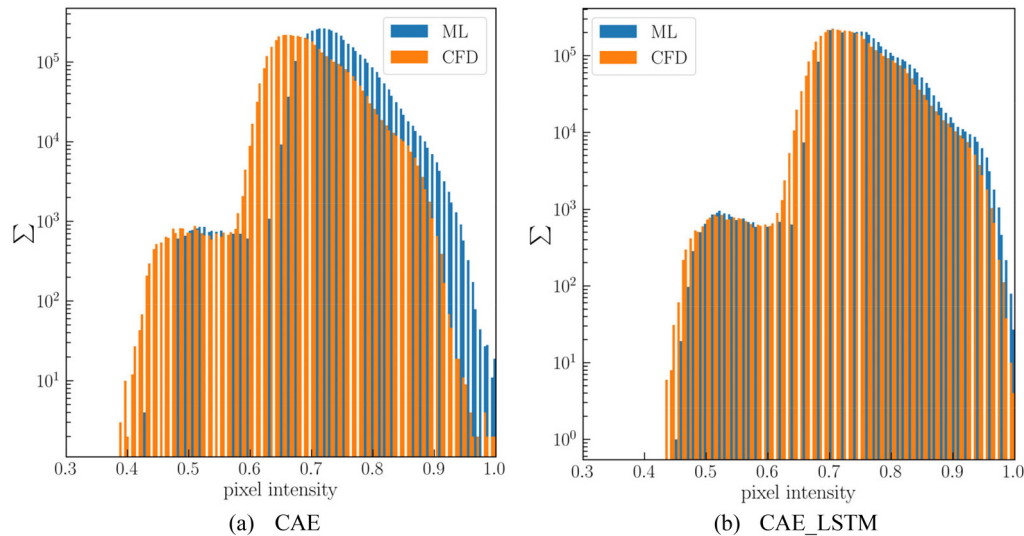
(a) CAE (b) CAE_LSTM

FIG. 27. Comparison of the histogram of the pixel intensity for (a) CAE and (b) CAE_LSTM architectures.

material and energy consumptions, enabling them to obtain high-quality, uniform and esthetic appeal film together with a higher range of transfer efficiency (TE). Employing heated nitrogen instead of air and using ERBS with mounted innovative HVRB and HVACR conductors lead to higher transfer efficiency (TE), rare overspray occurrence, formation of an esthetic paint film with higher quality, lower paint consumption, VOC emission, and application time. Comparative results proved that the ERBS with the novel HVRB conductor obtained significant improvement in spray pattern/droplet direction, film homogeneity/density and two critical metrics of the overall *TE* and average *SMD* with around 12.21% (from 71.7% to 83.9%) enhancement and 3.0% (from 6.25 to 5.9 μm) decrement compare to CES at the moderate voltage (-40 kV).

In the present work, a deep learning model is developed to enhance the prediction accuracy and reduce the computational time for two critical aspects of the Nitrotherm spraying flow dynamics. The considered machine learning model analyzes 2D images of the spray distributions captured from the side and top views, as well as LIC side snapshots of the Eulerian velocity field. Since our model is designed to work with 2D images, we opted for convolutional models and tested different architectures. The findings revealed that utilizing convolutional models, incorporating recurrence to the encoding/decoding layers, along with the use of LSTM cells for temporal inputs, aids in feature extraction. The predictions indicate that computation time can be reduced by around 90%. The final shape of the liquid deposition on the target is predicted with an error rate of only 1%. Additionally, the introduced model visualized the vortex structures implicit in the spray evolution under the applied external conditions with high precision. In review, our deep learning model has demonstrated the potential to enhance prediction accuracy and reduce computational time for flow dynamics cases.

ACKNOWLEDGMENTS

AUTHOR DECLARATIONS
Conflict of Interest

The authors have no conflicts to disclose.

Author Contributions

Mohammad-Reza Pendar: Conceptualization (lead); Data curation (lead); Formal analysis (lead); Investigation (lead); Methodology (lead); Supervision (lead); Validation (lead); Visualization (lead); Writing – original draft (lead); Writing – review & editing (lead). **Sílvio Cândido:** Formal analysis (supporting); Investigation (equal); Methodology (equal); Visualization (supporting); Writing – original draft (supporting); Writing – review & editing (supporting). **José Páscoa:** Funding acquisition (lead); Project administration (lead); Supervision (lead); Writing – review & editing (supporting).

DATA AVAILABILITY

The data that support the findings of this study are available on request from the authors.

REFERENCES

Ahmed, M. and Youssef, M. S., "Characteristics of mean droplet size produced by spinning disk atomizers," J. Fluids Eng. **134**(7), 071103 (2012).

Ahmed, M. and Youssef, M. S., "Influence of spinning cup and disk atomizer configurations on droplet size and velocity characteristics," Chem. Eng. Sci. **107**, 149–157 (2014).

08 September 2023 13:45:49

Akafuah, N. K., Poozesh, S., Salaimeh, A., Patrick, G., Lawler, K., and Saito, K., "Evolution of the automotive body coating process—A review," Coatings **6**(2), 24 (2016).

Arumugham-Achari, A. K., Grifoll, J., and Rosell-Llompart, J., "A comprehensive framework for the numerical simulation of evaporating electrosprays," Aerosol Sci. Technol. **49**(6), 436–448 (2015).

Bensalah, W., Loukil, N., Wery, M., and Ayedi, H. F., "Assessment of automotive coatings used on different metallic substrates," Int. J. Corrosion. **2014**, 838054.

Brentjes, A., Pozarlik, A. K., and Brem, G., "Numerical simulation of evaporating charged sprays in spray chilling," J. Electrostat. **107**, 103471 (2020).

Brunton, S. L., Proctor, J. L., and Kutz, J. N., "Discovering governing equations from data by sparse identification of nonlinear dynamical systems," Proc. Natl. Acad. Sci. U. S. A. **113**(15), 3932–3937 (2016).

Cooper, S. C, "Electrostatic fluid sprayer with active fluid cloud dispersal feature and method of electrostatic spraying," U.S. Patent No. 10,894,262 (ES Product Development LLC, 2021).

Darwish Ahmad, A., Abubaker, A. M., Salaimeh, A. A., and Akafuah, N. K., "Schlieren visualization of shaping air during operation of an electrostatic rotary bell sprayer: Impact of shaping air on droplet atomization and transport," Coatings **8**(8), 279 (2018).

Dastourani, H., Jahannama, M. R., and Eslami-Majd, A., "A physical insight into electrospray process in cone-jet mode: Role of operating parameters," Int. J. Heat Fluid Flow **70**, 315–335 (2018).

Dbouk, T. and Drikakis, D., "On coughing and airborne droplet transmission to humans," Phys. Fluids **32**(5), 053310 (2020).

De Villiers, E., *The Potential of Large Eddy Simulation for the Modeling of Wall Bounded Flows* (Imperial College of Science, Technology and Medicine, 2006).

Deng, Z., Chen, Y., Liu, Y., and Kim, K. C., "Time-resolved turbulent velocity field reconstruction using a long short-term memory (LSTM)-based artificial intelligence framework," Phys. Fluids **31**(7), 075108 (2019).

Domnick, J., Scheibe, A., and Ye, Q., "The simulation of electrostatic spray painting process with high-speed rotary bell atomizers," Part. Part. Syst. Charact. **23**(5), 408-416 (2006).

Domnick, J. and Thieme, M., "Atomization characteristics of high-speed rotary bell atomizers," Atomiz. Spr. **16**(8), 857 (2006).

Ellwood, K. R. and Braslaw, J., "A finite-element model for an electrostatic bell sprayer," J. Electrostat. **45**(1), 1–23 (1998).

Elsayed, K., and Lacor, C., "Modeling, analysis and optimization of aircyclones using artificial neural network, response surface methodology and CFD simulation approaches," Powder Technol. **212**(1), 115–133 (2011).

Gao, F., Zhang, Z., Jia, C., Zhu, Y., Zhou, C., and Wang, J., "Simulation and prediction of three-dimensional rotating flows based on convolutional neural networks," Phys. Fluids **34**, 095116(2022).

Ghosal, S., "An analysis of numerical errors in large-eddy simulations of turbulence," J. Comput. Phys. **125**(1), 187–206 (1996).

Im, K. S., Lai, M. C., Liu, Y., Sankagiri, N., Loch, T., and Nivi, H., "Visualization and measurement of automotive electrostatic rotary-bell paint spray transfer processes," J. Fluids Eng. **123**(2), 237–245 (2001).

Im, K. S., Lai, M. C., Yu, S.-T. J., and Matheson, R. R. Jr., , "Simulation of spray transfer processes in electrostatic rotary bell sprayer," J. Fluids Eng. **126**(3), 449–456 (2004).

Issa, R. I., "Solution of the implicitly discretised fluid flow equations by operator-splitting," J. Comput. Phys. **62**(1), 40–65 (1986).

Jackiw, I. M. and Ashgriz, N., "On aerodynamic droplet breakup," J. Fluid Mech. **913**, A33 (2021).

Kim, J., Kim, H., Kim, J., and Lee, C., "Deep reinforcement learning for large-eddy simulation modeling in wall-bounded turbulence," Phys. Fluids **34**(10), 105132 (2022).

Kingma, D. P. and Ba, J., "Adam: A method for stochastic optimization," arXiv:1412.6980 (2014).

Kochkov, D., Smith, J. A., Alieva, A., Wang, Q., Brenner, M. P., and Hoyer, S., "Machine learning–accelerated computational fluid dynamics," Proc. Natl. Acad. Sci. U. S. A. **118**(21), e2101784118 (2021).

LarKermani, E., Roohi, E., and Porté-Agel, F., "Evaluating the modulated gradient model in large eddy simulation of channel flow with OpenFOAM," J. Turbul. **19**(7), 600–620 (2018).

Liu, F., "A thorough description of how wall functions are implemented in OpenFOAM," in *Proceedings of CFD with OpenSource Software* (2016), p. 34.

Liu, J., Yu, Q., and Guo, Q., "Experimental investigation of liquid disintegration by rotary cups," Chem. Eng. Sci. **73**, 44–50 (2012).

Mondal, S. and Sarkar, S., "Multi-fidelity prediction of spatiotemporal fluid flow," Phys. Fluids **34**(8), 087112 (2022).

Moore, J. R., "Automotive paint application," in *Protective Coatings* (Springer, 2017), pp. 465–496.

Naphon, P., Wiriyasart, S., Arisariyawong, T., and Nakharintr, L., "ANN, numerical and experimental analysis on the jet impingement nanofluids flow and heat transfer characteristics in the micro-channel heat sink," Int. J. Heat Mass Transfer **131**, 329–340 (2019).

Nolte, H. J., Fischer, A., Marquardt, P., Berkowitsch, J., and Schneider, J., "Electrode assembly for an electrostatic atomizer," U.S. Patent No. 10,464,084 (Duerr Systems AG, 2019).

Oswald, W., Gödeke, L., Ehrhard, P., and Willenbacher, N., "Influence of the elongational flow resistance and pigmentation of coating fluids on high-speed rotary bell atomization," Atomiz. Spr. **29**(10), 913 (2019).

Patankar, S. V. and Spalding, D. B., "A calculation procedure for heat, mass and momentum transfer in three-dimensional parabolic flows," in *Numerical Prediction of Flow, Heat Transfer, Turbulence and Combustion* (Pergamon, 1983), pp. 54–73.

Pendar, M. R. and Páscoa, J. C., "Numerical modeling of electrostatic spray painting transfer processes in rotary bell cup for automotive painting," Int. J. Heat Fluid Flow **80**, 108499 (2019).

Pendar, M. R. and Páscoa, J. C., "Atomization and spray characteristics around an ERBS using various operational models and conditions: Numerical investigation," Int. J. Heat Mass Transfer **161**, 120243 (2020).

Pendar, M. R. and Páscoa, J. C., "Numerical analysis of charged droplets size distribution in the electrostatic coating process: Effect of different operational conditions," Phys. Fluids **33**(3), 033317 (2021).

Pendar, M. R., Rodrigues, F., Páscoa, J. C., and Lima, R., "Review of coating and curing processes: Evaluation in automotive industry," Phys. Fluids **34**(10), 101301 (2022).

Ranz, W. E. and Marshall, W. R., "Evaporation from drops," Chem. Eng. Progr. **48**(3), 141–146 (1952).

Ray, R., Henshaw, P., and Biswas, N., "Characteristics of spray atomization for liquid droplets formed using a rotary bell atomizer," J. Fluids Eng. **141**(8), 081303 (2019).

Roohi, E., Pendar, M. R., and Rahimi, A., "Simulation of three-dimensional cavitation behind a disk using various turbulence and mass transfer models," Appl. Math. Modell. **40**(1), 542–564 (2016).

SAMES Technology, see http://www.sames-kremlin.com for "employed ERBS designed and commercialized by SAMES" (2019) (last accessed 15 September 2019).

Shen, B., Ye, Q., Guettler, N., Tiedje, O., and Domnick, J., "Primary breakup of a non-Newtonian liquid using a high-speed rotary bell atomizer for spray-painting processes," J. Coat. Technol. Res. **16**(6), 1581–1596 (2019).

Shen, B., Ye, Q., Tiedje, O., and Domnick, J., "Primary breakup of liquids using a high-speed rotary bell atomizer for spray painting processes," in *ILASS Europe 28th European Conference on Liquid Atomization and Spray Systems* (Editorial Universitat Politècnica de València, 2017), pp. 355–361.

Shi, X., Chen, Z., Wang, H., Yeung, D. Y., Wong, W. K., and Woo, W. C., "Convolutional LSTM network: A machine learning approach for precipitation nowcasting," in *Advances in Neural Information Processing Systems* (NeurIPS, 2015), Vol. 28.

Shrimpton, J. S. and Laoonual, Y., "Dynamics of electrically charged transient evaporating sprays," Int. J. Numer. Methods Eng. **67**(8), 1063–1081 (2006).

Soma, T., Katayama, T., Tanimoto, J., Saito, Y., Matsushita, Y., Aoki, H., Nakai, D., Kitamura, G., Miura, M., Asakawa, T., Daikoku, M., Haneda, T., Hatayama, Y., Shirota, M., and Inamura, T., "Liquid film flow on a high speed rotary bell-cup atomizer," Int. J. Multiphase Flow **70**, 96–103 (2015).

Spang, P., "Applying paints with nitrogen," Int. Surf. Technol. **7**(1), 15–15 (2014).

Stevenin, C., Bereaux, Y., Charmeau, J. Y., and Balcaen, J., "Shaping air flow characteristics of a high-speed rotary-bell sprayer for automotive painting processes," J. Fluids Eng. **137**(11), 111304 (2015).

Terebessy, T., "Electrostatic atomizer, and method for electrostatically atomizing by use of the same," U.S. Patent No. 10,179,338 (Sumitomo Chemical Co Ltd., 2019).

Toljic, N., Adamiak, K., Castle, G. S. P., Kuo, H. H. H., and Fan, H. T., "Three-dimensional numerical studies on the effect of the particle charge to mass ratio distribution in the electrostatic coating process," J. Electrostat. **69**(3), 189–194 (2011).

Viti, V., Kulkarni, J., and Watve, A., "Computational fluid dynamics analysis of the electrostatic spray painting process with a rotating bell cup," Atomiz. Spr. **20**(1), 1–17 (2010).

Wang, S., Golden, J., and Kocher, C. G, "Method and apparatus for electrostatic spray," U.S. Patent No. 7,150,412 (Clean Earth Technologies LLC, 2006).

Wilson, J., Grib, S., Darwish Ahmad, A., Renfro, M., Adams, S., and Salaimeh, A., "Study of near-cup droplet breakup of an automotive electrostatic rotary bell (ESRB) atomizer using high-speed shadowgraph imaging," Coatings **8**(5), 174 (2018).

Yang, K. T., "Artificial neural networks (ANNs): a new paradigm for thermal science and engineering," J. Heat Transfer **130**(9), 093001 (2008).

Yasumura, K., Saito, Y., Shoji, M., Matsushita, Y., Aoki, H., Miura, T., Ogasawara, S., Daikoku, M., Shirota, M., and Inamura, T., "Development of quantitative evaluation method for droplet behavior with high speed rotary bell-cup atomizer," Kagaku Kogaku Ronbunshu **37**, 296–304 (2011).

Ye, Q., Domnick, J., and Khalifa, E., "Simulation of the spray coating process using a pneumatic atomizer," in ILASS-Europe, 9–11 September 2002.

Yousif, M. Z., Yu, L., and Lim, H. C., "High-fidelity reconstruction of turbulent flow from spatially limited data using enhanced super-resolution generative adversarial network," Phys. Fluids **33**(12), 125119 (2021).

Yousif, M. Z., Yu, L., and Lim, H. C., "Super-resolution reconstruction of turbulent flow fields at various Reynolds numbers based on generative adversarial networks," Phys. Fluids **34**(1), 015130 (2022).

Yousif, M. Z., Yu, L., Hoyas, S., Vinuesa, R., and Lim, H., "A deep-learning approach for reconstructing 3D turbulent flows from 2D observation data," Sci. Rep. **13**(1), 2529 (2023).

Zahiri, A. P. and Roohi, E., "Anisotropic minimum-dissipation (AMD) subgrid-scale model implemented in OpenFOAM: Verification and assessment in single-phase and multi-phase flows," Comput. Fluids **180**, 190–205 (2019).

08 September 2023 13:45:49